Computers and Structures 301 (2024) 107469

Contents lists available at ScienceDirect

Computers and Structures

journal homepage: www.elsevier.com/locate/compstruc

Minimizing the maximum von Mises stress of elastic continuum structures using topology optimization and additively manufactured functionally graded materials

Rui F. Silva [a,*], Pedro G. Coelho [a,b,c], Fábio M. Conde [a,c], Bernardo R. Santos [a], João P. Oliveira [d]

[a] UNIDEMI, Department of Mechanical and Industrial Engineering, NOVA School of Science and Technology, Universidade NOVA de Lisboa, Caparica 2829-516, Portugal
[b] IDMEC, Instituto Superior Técnico, Universidade de Lisboa, Av. Rovisco Pais 1, Lisbon 1049-001, Portugal
[c] Intelligent Systems Associate Laboratory, LASI, Guimarães 4800-058, Portugal
[d] CENIMAT/I3N, Department of Materials Science, NOVA School of Science and Technology, Universidade NOVA de Lisboa, Caparica 2829-516, Portugal

ARTICLE INFO

Keywords:
FGM
Structures
Multi-material
Topology
Optimization
Stress

ABSTRACT

The rising cost of natural resources and environmental concerns motivate systematic design and manufacture of more efficient structures. For that purpose, topology optimization has been appealing, as well as working on an enlarged design space to include multi-material solutions. The resulting optimal designs can be materialized using multi-material additive manufacturing. In the present framework, multi-material printed parts or layouts can be envisaged as having better strength properties than single-material counterparts.

The maximum von Mises stress is minimized inside a design domain through topology changes and material selection. The selected composite material model encompasses either the classical arrange of two discrete materials with sharp interfaces, or their mixture controlled by the volume fraction of each base material to generate a Functionally Graded Material (FGM). An optimized continuous variation of properties makes the FGM appealing to mitigate stress concentrations. To adequately capture the physics of mixtures considering the FGM's mechanical properties, one uses the RAMP interpolation scheme within the Hashin-Shtrikman bounds.

A set of plane stress benchmarks are proposed. It is shown that considerably lower stress peaks on the evaluated structures can be obtained on the account of introducing more than one solid phase, specifically in the case of FGM solutions.

1. Introduction

Nowadays, concerns on energy and environmental sustainability motivate multiple industrial sectors, such as the automotive and aerospace industries, to reduce structural weight taking advantage of efficient design tools such as Topology Optimization (TO), multi-material solutions and related additive manufacturing developments [62]. Since structurally feasible designs in practice also require low stress levels, stress-based TO is fundamental to assist the conceptual design stage, being the reason why TO formulations including stress as a constraint, or as an objective, have received increased attention in the community, more recently in the setting of multi-material design.

Since the pioneering work of Michell [60] and the seminal work of Bendsøe and Kikuchi [4], TO has been an active area of research in a wide range of industrial applications and advanced numerical studies, as detailed by Deaton and Grandhi [23]. In general, TO of solid structures involves the determination of the connectivity, number, location, and shape of holes (voids) inside a given design domain, for a given set of boundary conditions. Although TO may render very efficient design solutions, they often present geometrical complexity which challenges their manufacture. In fact, the current state-of-the-art on available manufacturing technologies may prevent attaining the extreme (optimal) predicted performance levels obtained by TO [64]. Due to the discrete nature of the original TO problem, density-based interpolation schemes like SIMP (Solid Isotropic Material with Penalization) and RAMP (Rational Approximation of Material Properties) have been developed. These schemes transform the original problem into a continuous one. The SIMP model [5] has gained prominence due to its simplicity and computational efficiency. It has become the dominant density-based TO approach in both the literature and industrial

* Corresponding author.
E-mail address: rmfd.silva99@gmail.com (R.F. Silva).

https://doi.org/10.1016/j.compstruc.2024.107469
Received 26 September 2023; Accepted 25 June 2024
Available online 8 July 2024

applications [69,70,20,51]. In a nutshell, the SIMP scheme introduces some sort of penalty on continuous artificial density-based design variables that steers the solution to discrete 0–1 values. The RAMP material model was originally proposed to alleviate non-concavity of the original SIMP interpolation scheme [78]. The primary difference between RAMP and SIMP material models is that, unlike SIMP, RAMP has non-zero sensitivity at zero density. This means that, as material is removed and turns into void during the optimization process, recovering that material from void is far more complicated when using SIMP than RAMP. This feature makes the RAMP model preferred for problems related to very low density values in the presence of design dependent loading, as self-weight [12] and thermal loads [28].

At this point, the pursuit of Single-Material Topology Optimization (SMTO) has reached a state of diminishing returns. Multi-Material Topology Optimization (MMTO) has been widely investigated lately and it consists in applying the classical TO methods adapted to design structures with multiple materials, optimizing both the structural layout and the distribution of materials across the layout. In the literature of MMTO, one finds that the major focus has been on the structural compliance minimization problem subject to constraints on the volume fraction of material phases [52,53]. However, besides the volume fraction constraints, constraints on mass [40,88,72,45] and material cost [94] have also been addressed. Moreover, the weight minimization problem within the multi-material framework has been considered preferable in engineering practice, see e.g., Long et al. [55], Lu et al. [56], Jung et al. [42].

The impact of research on purely compliance-based TO problems can be questioned. In many industrial applications, it is of central importance to control the highly stressed regions (stress concentration regions) inside composite structural components since they are most likely the first to fail during service. Therefore, this motivates authors to pursue a strength-oriented (stress-based) MMTO. Stress-based TO is challenging mainly due to: (1) the singularity phenomenon; (2) the local nature of stresses; and (3) the highly nonlinear stress behavior. Some prior contributions have properly dealt with these aspects, see e.g., Cheng and Guo [13], Duysinx et al. [26,27], Bruggi [9], Le et al. [50], París et al. [65,66], Holmberg et al. [38]. Furthermore, when minimizing stresses, the unwanted best (trivial) solution is no structure [77]. In the multi-material setting, these challenges correspond to an increased level of complexity. The topic of strength-oriented MMTO is still an open problem. So far, the existing stress-constrained formulations have mainly dealt with objectives such as compliance minimization [35,39,58] and volume/mass minimization [68,44,57,90,49]. Among these objectives, the maximum stress minimization is another challenging one. Yet, it has been investigated to a much lesser extent [33,17].

Recently, interest has also arisen on the subject of optimal design resorting to Functionally Graded Materials (FGMs). FGMs were introduced in the late 1980s in Japan by a group of materials scientists as a new class of advanced composite materials, whose equivalent properties vary continuously as a known function along one (or more) direction(s) to obtain a modified response to external loadings [48,63]. The idea of creating structures with graded properties is bioinspired, as the most impressive (efficient) FGMs can be found as masterpieces in nature [61,16,71]. This gradient feature is a breakthrough on creating structural parts capable of better reducing stress concentrations (singularities), which often arise due to geometrical perturbations to meet construction requirements such as the insertion of holes, depressions, corners or fillets. Choosing a suitable variation of material properties is critical to excel on attaining stress maps showing lower magnitudes, as reported in the literature [91,73,74,92,31,32]. FGMs have the potential of outperforming conventional composites in reducing stress concentrations, which can be even better explored employing optimization techniques to predict variations on material properties across the entire solid domain, amidst void areas, as addressed in the present framework.

The versatility of FGM designs makes them a “perfect” candidate for optimization problems, greatly enlarging the design space. TO extensions to the multi-material setting are quite appealing and can be appropriately adapted to also accommodate structural design based on FGMs. Up to the authors’ knowledge, the first attempt to obtain FGM design solutions using TO is the work of Xia and Wang [89]. These authors used a volume fraction model of material composition and average the Hashin-Shtrikman (HS) bounds to compute the effective isotropic material elastic modulus, at each design finite element, and the problem objective function was the sum of mean compliance. In this original work, as in others since then [25,83,18], the FGM is seen as an extensive smooth variation of material properties on account of varying composition’s volume fractions throughout the design domain allowing simultaneous layout optimization. In such works, the mixture of two distinct materials prevails extensively over their discrete distribution. This is the same type of FGM addressed in the present framework. Besides this, it is also noteworthy to recall from the literature that an FGM can also be created on account of the spatial variation of porosity or micro-architecture in the case of materials with microstructure, see Radman et al. [67]. Furthermore, another interesting type of FGM solution created is only at interface regions (transition zones) in conventional composites, i.e., locally one creates smooth variations between the properties of two neighboring solid material regions, for which the level-set based TO has been successfully applied [86,43,34].

Just a few stress-based formulations coupled with FGMs are found in the literature. As regards macrostructural design, the readers are referred to Lipton [54], Stump et al. [79], Conlan-Smith and James [19] and Tamijani [84]. As regards microstructural design, examples can be found on Alacoque et al. [1] and Conde et al. [17]. However, it should be noted that the spatial variation on elastic properties of the FGMs may raise manufacturability issues. The pioneer work of Ituarte et al. [41] elaborates on a workflow that integrates FGM optimal design, manufacturing and characterization of polymeric parts. This future trend of combining TO with emerging additive manufacturing technologies enables the integrated design and fabrication of novel composites as FGMs with unprecedented performances, see Meng et al. [59].

The present paper focus is to extend the microscale framework presented in Conde et al. [17] to macrostructures (as beams and plates) properly adapting the stress-based TO problem using FGMs. Exploring FGMs in the frame of stress redistribution/reduction is adequately handled by TO and of engineering practical interest, especially on the macroscale where more demand for design solutions may exist and manufacturability may become easier. Therefore, the present work addresses a density-based MMTO in macrostructural design, considering two homogenous solids plus void. Basically, a stress-based MMTO is carried out such that the maximum von Mises stress is minimized under compliance and volume fraction constraints. Two different bi-material interpolation laws are proposed, rendering each one different design solutions. On one hand, one gets discrete material designs with material properties assumed to be discontinuous across the interface between adjacent material phases (sharp interfaces). On the other hand, one gets FGM designs using a material model based on the HS bounds, i.e., the theoretical bounds that provide a range of effective properties achievable for a certain volume fraction of the mixture between two isotropic materials. In the first case, it is expected that the resulting sharp interfaces between the two homogeneous solid phases are the zones of the domain with higher stress gradients. Furthermore, there is a stress discontinuity in the interface between two material phases, and the peak stress in the structure is expected to be there. A continuous gradation of material properties in the vicinity of the interface region between discrete materials results in an improved design solution. However, to completely explore the FGM potential in stress mitigation, one aims here to extend the FGM solution to the full-design domain, this way a uniformly stressed structure is favored. Lastly, the FGM designs are here compared with their multi-material and single-material counterparts to realize the strength benefits.

The paper is outlined as follows. Section 2 discusses the material

model, i.e., the related mathematical formulations of an elastic structure and the density-based multi-material interpolation schemes. Section 3 elaborates on the mathematical statement of the proposed formulation, on the sensitivity analysis with respect to (w.r.t.) design variables and on the computational implementation based on the Fortran programming language. In Section 4, the application of the stress-based formulation to numerical examples is presented. The numerical results are discussed in Section 5. Finally, concluding remarks are pointed out in Section 6.

2. Material model

Consider in Fig. 1 an arbitrary elastic body in two dimensions subjected to an externally applied traction load $\mathbf{t}$ on the boundary segment $\Gamma_t \subset \partial\Omega$ of the reference domain Ω, as well as fixed displacement boundary conditions on segment Γ_u. Consider two distinct subdomains of Ω. One is the design subdomain, Ω^{d} (in gray), where the topology and material distribution are to be determined from optimization. Another is the non-design subdomain, Ω^{nd}, which can be either void (white) or solid (black).

For an elastic problem, the stress–strain relation is known as:

$$\sigma_{ij} = E_{ijkl}\varepsilon_{kl} \tag{1}$$

where $\boldsymbol{\sigma}$ is the stress tensor, $\mathbf{E}$ is the stiffness tensor and $\boldsymbol{\varepsilon}$ is the Cauchy infinitesimal strain tensor defined by:

$$\varepsilon_{ij} = \frac{1}{2}\left(\frac{\partial u_i}{\partial x_j} + \frac{\partial u_j}{\partial x_i}\right) \tag{2}$$

where $\mathbf{u}$ is the displacement field and $\mathbf{x}$ is the position vector. The stiffness tensor $\mathbf{E}$ is assumed isotropic and depends on the design variables (artificial densities) through a bi-material interpolation law at a given point of the reference domain Ω. As further detailed in this section, the material model considers two different density-based interpolation schemes to accomplish different types of material distributions. In mechanical design, several failure metrics are commonly applied to generalize material failure to states of combined normal (tension and compression) and shear stresses. In the present work, one uses the common von Mises failure criterion. Let the reference domain $\Omega = \Omega^{\mathrm{d}} \bigcup \Omega^{\mathrm{nd}}$ be discretized in N 8-node quadrilateral Finite Elements (FEs), as illustrated in Fig. 1. Considering each element $e = 1, 2, \ldots, N$ of Ω to have a volume (area in 2D) of $|\Omega_e|$, the von Mises stress σ_e^{VM} for a plane stress problem, assumed uniform in each $|\Omega_e|$, is computed as the volume average of the von Mises stresses, calculated at the 2x2 integration Gauss points of the FE, i.e.,

$$\sigma_e^{\mathrm{VM}} = \frac{\int_{\Omega_e} \sqrt{\frac{1}{2}\left[(\sigma_{11}^e - \sigma_{22}^e)^2 + (\sigma_{11}^e)^2 + (\sigma_{22}^e)^2\right] + 3(\sigma_{12}^e)^2}\,\mathrm{d}\Omega_e}{|\Omega_e|} \tag{3}$$

where σ_e^{VM} depends explicitly on $\boldsymbol{\sigma}$. One gets the displacements $\mathbf{u}$ solving the linear static equilibrium equation ($\mathbf{Ku} = \mathbf{F}$) and then the strain tensor (2), the stress tensor (1) and the von Mises stress (3) for each element e are postprocessed.

The present work developments are based upon MMTO. One considers up to two base solid phases plus void (total of 3 phases), such that either discrete (classical MMTO) or graded material (FGMTO) design solutions can be obtained. To solve both MMTO and FGMTO problems considering this number of different base material phases, one explores established interpolation schemes, i.e., SIMP and RAMP. In fact, a combination of schemes is explored. To address the MMTO problem one follows the conventional approach of recursive SIMP [6], here called SIMP-SIMP, while a combination of SIMP and RAMP appears to be more suitable to the intended physical interpretation of FGM solutions, so-called SIMP-RAMP here. Considering two base isotropic materials, besides void, the predicted material stiffness tensor based on the proposed multi-material interpolation schemes, SIMP-SIMP and SIMP-RAMP, is expressed as follows, respectively:

$$\mathbf{E} = (\rho_1)^{p_1}\left[(\rho_2)^{p_2}\mathbf{E}_1 + \left(1 - (\rho_2)^{p_2}\right)\mathbf{E}_2\right] \tag{4}$$

$$\mathbf{E} = (\rho_1)^{p_1}\left[\frac{\rho_2}{1 + q(1-\rho_2)}\mathbf{E}_1 + \left(1 - \frac{\rho_2}{1 + q(1-\rho_2)}\right)\mathbf{E}_2\right] \tag{5}$$

where $\rho_1, \rho_2 \in [\rho_{\min}, 1]$ are the artificial densities for layout and material selection purposes, respectively. Furthermore, p_1 and p_2 are the SIMP penalization exponents and q is the RAMP penalization parameter. Regarding density ρ_1, the topology design variable, a common SIMP penalization exponent is utilized, i.e., $p_1 \geq 3$ in 2D problems (see [7]), making intermediate values unfavorable such that "black-white" designs can be identified. The lower bound of the design variables, $\rho_{\min}$, is set to be small enough (10^{-3}) to prevent singularity issues in the FE model. Finally, $\mathbf{E}_1$ and $\mathbf{E}_2$ are the stiffness tensors of the strong and weak solid phases, respectively. Therefore, the schemes (4) and (5) interpolate among void (blue), stiffer solid $\mathbf{E}_1$ (red), and weaker solid $\mathbf{E}_2$ (green), as sketched in Fig. 1. The vertical color map at the right side of Fig. 1 illustrates the possible range of material properties when the mixture of solid phases, $\mathbf{E}_1$ and $\mathbf{E}_2$, is allowed to generate an FGM design solution.

Both SIMP and RAMP interpolation schemes succeed in compliance minimization problems. However, in the context of purely mechanical load problems, the relative insensitivity of the SIMP scheme at zero

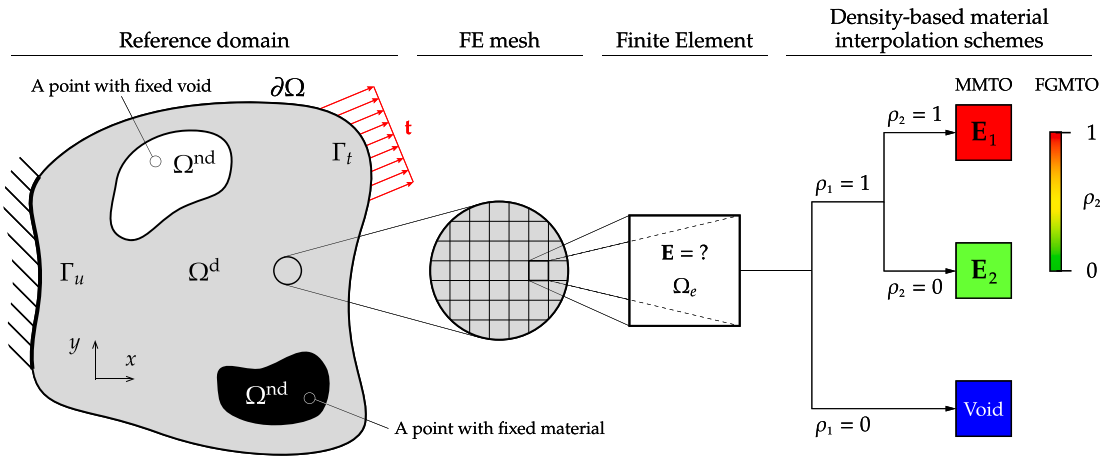

Fig. 1. Arbitrary two-dimensional elastic continuous structural domain $\Omega = \Omega^{\mathrm{d}} \bigcup \Omega^{\mathrm{nd}}$ with schematic representation of MMTO and FGMTO density interpolation schemes.

density was reported to be advantageous when solving stress-based TO problems, as shown by Deaton and Grandhi [24]. Furthermore, the RAMP interpolation scheme satisfies the HS bounds for two-phase materials [78]. This is here seen as an advantage for the FGMTO problem modelling, where the SIMP is comparatively limited [17]. As a result, the proposed SIMP-RAMP scheme (5) takes advantage of SIMP for the layout definition purpose and RAMP for the material selection purpose. As regards the SIMP-SIMP scheme in (4), the intermediate ρ_2 values have no physical meaning. Therefore, ρ_2 should be steered to 0–1 values at the end of the design iterations, so a unique phase (among three) is pointwisely selected according to the combination of values between the two artificial variables, ρ_1 and ρ_2, see Fig. 1 right side. To promote discrete material solutions, one uses equal penalizations, i.e., $p_1 = p_2$. As regards the SIMP-RAMP scheme in (5), q must be carefully chosen to add physical meaning to intermediate ρ_2 densities in the context of FGMs.

In a functionally graded structure, one expects material properties varying continuously, unlike composites embedding distinct solid (uniform) phases presenting sharp interfaces. Moreover, the solid that results from the mixture of two base solids exhibits material properties that can be theoretically approximated by mixture rules, in terms of the volume fractions of constituent materials, respecting the physics of solid mixtures. Quite a few mixture rules can be found in the literature [36,80,82]. Since the present work is focused on the optimal design of structures, one chooses to use the HS bounds for the elastic moduli of isotropic composite materials. The HS bounds depend on the volume fractions of each constituent materials, while assuming they are mixed uniformly with no microstructure (homogeneous resulting solid). In the FGMTO setting, the intermediate values of ρ_2 represent then the percentage of each solid phase ($\mathbf{E}_1$ and $\mathbf{E}_2$) present in the solid mixture, at a given point in the domain, and must be consistent with these bounds. Assuming a 2D problem, that both constituent materials are isotropic, together with their mixture, and both have the same Poisson's ratio, equal to 1/3, the upper and lower bound of HS, $E^{\mathrm{u}}_{\mathrm{HS}}$ and $E^{\mathrm{l}}_{\mathrm{HS}}$, respectively, depending on ρ_2, read as follows [6]:

$$E^{\mathrm{u}}_{\mathrm{HS}} = \frac{\rho_2 E_1 + (3-\rho_2)E_2}{(3-2\rho_2)E_1 + 2\rho_2 E_2} E_1 \tag{6}$$

$$E^{\mathrm{l}}_{\mathrm{HS}} = \frac{(2+\rho_2)E_1 + (1-\rho_2)E_2}{2(1-\rho_2)E_1 + (1+2\rho_2)E_2} E_2 \tag{7}$$

where $\rho_2 \in [\rho_{\min}, 1]$ represents the volume fraction of the strong constituent material E_1 (Young's Modulus), while $(1-\rho_2)$ is the volume fraction of the weak constituent material E_2. Therefore, regarding FGM structures, the penalization parameter q in (5) requires careful choice, such that the solid mixture at stake be consistent with physics and thus adequately capturing the FGM theoretical properties. Following-up the work previously developed by Conde et al. [17], one realizes that a power-law-based interpolation scheme, like SIMP, will never accurately satisfy the HS bounds for the ρ_2 density range, since SIMP has zero sensitivity at zero density while the derivative of (7) is positive at this same point. Alternatively, the RAMP interpolation scheme renders a curve falling within the rigorous bounds of HS, choosing q from the interval $2(E_1 - E_2)/(E_1 + 2E_2) \leq q \leq 2(E_1 - E_2)/(3E_2)$ for materials with Poisson's ratio equal to 1/3, see Stolpe and Svanberg [78]. In the present framework, one chooses $q = 1.04$ which approximates, without much loss of accuracy, the average of the upper (6) and lower (7) HS bounds, considering material properties given in Table 2 (Section 4). The resulting RAMP curve is plotted in Fig. 2. If the exact average curve is aimed, one should consider q as a function of ρ_2. However, that would complicate sensitivities. The RAMP derivative is straightforward considering q fixed.

Bear in mind the following hypothesis of the adopted material model. On one hand, in case distinct material phases are aimed, it is assumed that they are rigidly bounded, meaning a perfect material-

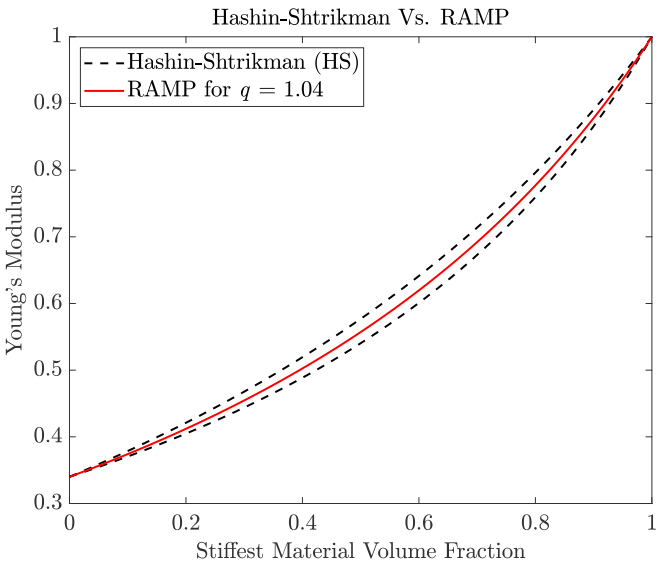

Fig. 2. Plot of the Hashin-Shtrikman bounds and RAMP interpolation scheme, for two different isotropic materials.

material interface. In practice, the material attaining its yield stress is only one of the ways a composite material can fail, as delamination is one of the most notorious failure modes. On the other hand, in case FGM solutions are sought, it is assumed that the mixture of both solid materials is possible for the entire volume fraction range (or composition percentages), which in reality can be questioned when the two different materials may have too distinct properties. This issue is potentially prevalent in metallic alloys when these are the basis for FGM production due to the potential metallurgical incompatibilities, but is significantly less impactful when using polymers. Furthermore, the material model also assumes linear elasticity, and ductile solids, such that failure can be predicted by the von Mises stress criterion.

3. Optimization problem

The minimization of the maximum equivalent stress (min–max σ^{VM}) is adopted here, as it better explores the FGM potential in stress mitigation. The "bound formulation" is used here (see Taylor and Bendsøe [85]) to circumvent the non-differentiability of min–max problems. This strategy formulates an equivalent problem by minimizing an artificial variable $\varkappa$, that replaces the non-differentiable functional max σ^{VM}, while every value of the equivalent stress is also constrained by $\varkappa$, i.e., $\sigma^{\mathrm{VM}}_e \leq \varkappa$. This way, the artificial variable $\varkappa$ can be minimized, enforcing along design iterations that all the stresses in the FE mesh get below $\varkappa$. Bound $\varkappa$ is thus a stress limit and a design variable in addition to the original density-based design variables, with $\varkappa \in]0, +\infty[$. Although the additional constraints in the problem statement demand more computational power, they impose a local stress constraint on every element of the FE mesh, meaning that stresses are treated as they are, i.e., local in nature. Another relevant approach when dealing with a huge number of stress constraints, that has proved to be computationally efficient, is the so-called stress aggregation-free approach, where all local stress constraints are handled by means of the augmented Lagrangian method, see e.g., Senhora et al. [75], Giraldo-Londono and Paulino [29,30], Giraldo-Londono et al. [30,29] and da Silva et al. [21].

The TO problem formulation used to obtain FGM solutions with improved strength is presented in Section 3.1. In order to use a gradient-based optimization algorithm (MMA, [81]), first-order derivatives of all functions need to be computed, as detailed in Section 3.2. Lastly, the algorithm implemented to solve the optimization problem is summarized in Section 3.3.

3.1. Problem formulation

A density filter [11] is applied to both design variables, $\boldsymbol{\rho}_1$ and $\boldsymbol{\rho}_2$, to obtain $\widetilde{\boldsymbol{\rho}}_1$ and $\widetilde{\boldsymbol{\rho}}_2$. Hence, equations (4) and (5) are to be interpreted as depending on these filtered densities, since the structure layout is based upon them. Consequently, the original design variables $\boldsymbol{\rho}$ are assumed to have no physical meaning. Both $\boldsymbol{\rho}$ and $\widetilde{\boldsymbol{\rho}}$ are assumed uniform at each FE e. In the absence of the density filter, jagged boundaries (or interfaces) could be obtained due to the use of square-grid FE meshes, leading to stress singularities. Thereafter, the density filter promotes a contour smoothness on stress distributions, especially at curved boundaries.

The proposed stress-based problem formulation (11) is to be interpreted in the context of FGMTO, using two solids plus void, and thereafter is properly adapted to both MMTO and SMTO for comparison purposes.

$$\min_{\boldsymbol{\rho}_1,\boldsymbol{\rho}_2,\mathscr{z}} \quad \mathscr{z} \tag{11a}$$

$$\text{s.t.} \frac{\sigma_e^{\text{VM}}}{\mathscr{z}} \leq 1, e = 1, \cdots, N^{\text{d}} \tag{11b}$$

$$\frac{C}{C^*} \leq 1 \tag{11c}$$

$$\frac{V}{V^*} = \frac{\sum_{e=1}^{N^{\text{d}}} \left[\widetilde{\rho}_{1,e} \left|\Omega_e^{\text{d}}\right|\right]}{\left|\Omega^{\text{d}}\right| V^*} \leq 1 \tag{11d}$$

$$\frac{\varphi_1}{\zeta_1} = \frac{\sum_{e=1}^{N^{\text{d}}} \left[\left(1-\widetilde{\rho}_{1,e}\right)\left(\widetilde{\rho}_{1,e}-\rho_{\min}\right)\right]}{\zeta_1} \leq 1 \tag{11e}$$

where the design variables ρ_1, ρ_2 are within the intervals defined in Section 2; C is the compliance with an upper bound C^*; V^* is the upper bound on material volume fraction V; φ_1 measures the level of intermediate values (gray) present on the filtered density field $\widetilde{\boldsymbol{\rho}}_1$, and $\zeta_1 \in]0, +\infty[$ is its respective upper bound; N^{d} is the number of design elements present in the FE mesh. Additionally, as the present work considers the min–max stress problem, that one solves here resorting to the bound formulation (see also [15,17]), and not the stress-constrained problem based on the allowable stress definition, no stress singularity issues arise and thus no relaxation approach [13,9] is applied to (11b). Even so, the algorithm can remove material while solving (11). Finally, all constraints are written according to the input format of constraints as adopted by MMA (Fortran version), i.e., $g \leq 1$.

The compliance constraint (11c) must be imposed to prevent trivial solutions, as structure absence or uniform intermediate density rendering uniform stress [10,77]. The upper bound C^* definition is based upon the solution of the single-material compliance minimization problem under volume constraint only (SMTO), typically using the stiffest solid phase as base material. Then, in the multi-material stress-based problem, C^* is higher than the optimal C found by SMTO. This way an increased design freedom regarding material choice is given to the algorithm to reduce stresses at the expense of stiffness comparing to SMTO. Since the compliance is relaxed, the exponent p_1 in (5) may not be sufficient to penalize the intermediate densities (gray). Therefore, constraint (11e) is proposed to limit the amount of $\widetilde{\boldsymbol{\rho}}_1$ intermediate values, such that solid-void regions can be clearly identified. Note that intermediate density values of $\widetilde{\boldsymbol{\rho}}_2$ (material selection variables) hold physical meaning, i.e., an intermediate value defines the percentage of each solid phase present in the uniform solid mixture, see Section 2. The parameter ζ_1 in (11e) is problem dependent, thus it requires fine-tuning while running the same problem a few times.

When MMTO is aimed, the two following constraints are added to (11):

$$2 - \frac{V_2}{V_2^*} = 2 - \frac{\sum_{e=1}^{N^{\text{d}}} \left[\widetilde{\rho}_{1,e}\left(1-\widetilde{\rho}_{2,e}\right)\left|\Omega_e^{\text{d}}\right|\right]}{\left|\Omega^{\text{d}}\right| V_2^*} \leq 1 \tag{11f}$$

$$\frac{\varphi_2}{\zeta_2} = \frac{\sum_{e=1}^{N^{\text{d}}} \left[\left(1-\widetilde{\rho}_{2,e}\right)\left(\widetilde{\rho}_{2,e}-\rho_{\min}\right)\right]}{\zeta_2} \leq 1 \tag{11g}$$

where V_2 is the volume fraction of phase $\mathbf{E}_2$ and V_2^* is its minimal amount allowed in the design. In the context of MMTO, prescribing the amount of the softer solid $\mathbf{E}_2$ might be questionable, as the algorithm should be able to distribute this phase over the design domain in a manner that effectively reduce stresses, without the need of explicitly prescribing its amount. However, unless a minimal amount of phase $\mathbf{E}_2$ is enforced, the algorithm will always privilege intermediate densities (FGM-like solution) up to the limit set by the threshold ζ_2 in (11g). Regarding the intermediate density constraint (11g), it follows the same rationale behind (11e), but now applied to $\widetilde{\boldsymbol{\rho}}_2$ density variables, such that only the original discrete material phases are present amidst void. To facilitate problem convergence, the value of ζ_2 in (11g) is intentionally adjusted to be slightly higher than the minimum strictly required, thus some "gray" can be accommodated within the design, as will be seen later in Section 4.

3.2. Sensitivity analysis

Since problem (11) is solved by a gradient-based optimizer (MMA), a sensitivity analysis is needed. To obtain consistent sensitivities, the sensitivity of each function, say g, w.r.t. a change in design variables $\boldsymbol{\rho}$ is found by the use of the chain rule [76]:

$$\frac{\mathrm{d}g}{\mathrm{d}\rho_{j,e}} = \sum_{i\in N_e} \frac{\partial g}{\partial \widetilde{\rho}_{j,i}} \frac{\mathrm{d}\widetilde{\rho}_{j,i}}{\mathrm{d}\rho_{j,e}} = \sum_{i\in N_e} \frac{\partial g}{\partial \widetilde{\rho}_{j,i}} \left[\frac{r_{\min} - \|\mathbf{y}_e - \mathbf{y}_i\|}{\sum_{j\in N_i} \max\left\{0, r_{\min} - \left\|\mathbf{y}_j - \mathbf{y}_i\right\|\right\}}\right], \forall j \in \{1,2\} \tag{12}$$

where N_e is the neighborhood of element e and $r_{\min}$ is the filter radius which is set here to collect for averaging only the 8 adjacent element neighbors of element e, in 2D problems.

The required gradients in (12) w.r.t. $\widetilde{\rho}_{j,i}$ to solve the problems just presented in Section 3.1 are shown below. Bear in mind also that all sensitivities w.r.t. the design variables $\widetilde{\rho}_{j,i}$ are written below assuming a FE discretization of the reference domain Ω. Therefore, in the equations below, index $j \in \{1,2\}$ defines the corresponding density field (i.e., $\widetilde{\boldsymbol{\rho}}_1$ or $\widetilde{\boldsymbol{\rho}}_2$), each density is assumed constant within each element of the mesh, indexes $i, e \in \{1, \cdots, N^{\text{d}}\}$ correspond to the design FE index, index $l \in \{1, 2\}$ defines the respective functions φ_1 and φ_2, and indexes $z, y, k, m \in \{1, 2\}$ are related to the coordinate system directions considering 2D problems. The von Mises stress sensitivity is calculated through the adjoint method [37]. Derivatives w.r.t. the design variable $\mathscr{z}$ are trivial and, therefore, skipped here.

The compliance derivative is

$$\frac{\mathrm{d}C}{\mathrm{d}\widetilde{\rho}_{j,i}} = -\frac{1}{2} \frac{\partial E_{zykm}}{\partial \widetilde{\rho}_{j,i}} \int_{\Omega_i^{\text{d}}} \varepsilon_{km} \varepsilon_{zy} \, \mathrm{d}\Omega_i^{\text{d}} \tag{13}$$

The volume fraction derivative is

$$\frac{\mathrm{d}V}{\mathrm{d}\widetilde{\rho}_{j,i}} = \begin{cases} \dfrac{\left|\Omega_i^{\text{d}}\right|}{\left|\Omega^{\text{d}}\right|} & \text{if } j = 1 \\ 0 & \text{if } j = 2 \end{cases} \tag{14}$$

The material 2 volume fraction derivative is

$$\frac{\mathrm{d}V_2}{\mathrm{d}\widetilde{\rho}_{j,i}} = \begin{cases} \dfrac{(1-\widetilde{\rho}_{2,i})\left|\Omega_i^{\mathrm{d}}\right|}{\left|\Omega^{\mathrm{d}}\right|} & \text{if } j=1 \\ \dfrac{-\widetilde{\rho}_{1,i}\left|\Omega_i^{\mathrm{d}}\right|}{\left|\Omega^{\mathrm{d}}\right|} & \text{if } j=2 \end{cases} \tag{15}$$

The penalization function derivative is

$$\frac{\mathrm{d}\varphi_l}{\mathrm{d}\widetilde{\rho}_{j,i}} = \begin{cases} -2\widetilde{\rho}_{j,i} + \rho_{\min} + 1 & \text{if } j=l \\ 0 & \text{if } j\neq l \end{cases} \tag{16}$$

The total derivative of the von Mises stress, $\sigma_e^{\mathrm{VM}} = \sigma_e^{\mathrm{VM}}(\widetilde{\boldsymbol{\rho}}, \mathbf{u}(\widetilde{\boldsymbol{\rho}}))$, at element e, depends explicitly and implicitly on the design variable $\widetilde{\rho}_{j,i}$, such that:

$$\frac{\mathrm{d}\sigma_e^{\mathrm{VM}}}{\mathrm{d}\widetilde{\rho}_{j,i}} = \frac{\partial\sigma_e^{\mathrm{VM}}}{\partial\widetilde{\rho}_{j,i}} + \frac{\partial\sigma_e^{\mathrm{VM}}}{\partial u_k}\frac{\mathrm{d}u_k}{\mathrm{d}\widetilde{\rho}_{j,i}} \tag{17}$$

In the Finite Element Method (FEM), the displacements in nodes $\mathbf{u}$ are multiplied by shape functions ϕ in order to estimate the displacement at any point in the domain of the considered element:

$$u_k = \overline{u}_{k\alpha}\phi_\alpha \tag{18}$$

where $\alpha \in \{1, \cdots, 8\}$ is the node number of the 8-node isoparametric quadrilateral FE (Q8) used here. The total derivative of u_k w.r.t. $\widetilde{\rho}_{j,i}$ in (17) can be rewritten in terms of the equilibrium equation derivative, here handled in its discrete form ($\mathbf{Ku} = \mathbf{F}$), i.e.,

$$\frac{\mathrm{d}\sigma_e^{\mathrm{VM}}}{\mathrm{d}\widetilde{\boldsymbol{\rho}}} = \frac{\partial\sigma_e^{\mathrm{VM}}}{\partial\widetilde{\boldsymbol{\rho}}} + \boldsymbol{\lambda}^{\mathrm{T}}\left[\frac{\partial\mathbf{F}}{\partial\widetilde{\boldsymbol{\rho}}} - \frac{\partial\mathbf{K}}{\partial\widetilde{\boldsymbol{\rho}}}\mathbf{u}\right] \tag{19}$$

where vector $\boldsymbol{\lambda}$ is the adjoint variable (or so-called dummy load vector) that solves the following adjoint problem:

$$\mathbf{K}\boldsymbol{\lambda} = \left(\frac{\partial\sigma_e^{\mathrm{VM}}}{\partial\mathbf{u}}\right)^{\mathrm{T}} \tag{20}$$

Moreover, the load vector $\mathbf{F}$ is here considered density-independent implying that its derivative in (19) vanishes. Recovering index notation, the von Mises stress derivative w.r.t. displacements $\mathbf{u}$ in (20) is given by:

$$\frac{\partial\sigma_e^{\mathrm{VM}}}{\partial\overline{u}_{k\alpha}} = \frac{\int_{\Omega_e^{\mathrm{d}}}\frac{1}{2}\left[\left(\frac{\partial\sigma_{11}^e}{\partial\overline{u}_{k\alpha}} - \frac{\partial\sigma_{22}^e}{\partial\overline{u}_{k\alpha}}\right)\left(\sigma_{11}^e - \sigma_{22}^e\right) + \frac{\partial\sigma_{11}^e}{\partial\overline{u}_{k\alpha}}\sigma_{11}^e + \frac{\partial\sigma_{22}^e}{\partial\overline{u}_{k\alpha}}\sigma_{22}^e + 6\frac{\partial\sigma_{12}^e}{\partial\overline{u}_{k\alpha}}\sigma_{12}^e\right]\mathrm{d}\Omega_e^{\mathrm{d}}}{\left|\Omega_e^{\mathrm{d}}\right|\sqrt{\frac{1}{2}\left[\left(\sigma_{11}^e - \sigma_{22}^e\right)^2 + \left(\sigma_{11}^e\right)^2 + \left(\sigma_{22}^e\right)^2\right] + 3\left(\sigma_{12}^e\right)^2}} \tag{21}$$

In order to compute the von Mises stress derivative w.r.t. displacements (21), the stress–strain relation (1) derivative w.r.t. displacements must be computed first, which gives:

$$\frac{\partial\sigma_{zy}^e}{\partial\overline{u}_{k\alpha}} = E_{zykm}\frac{\partial\varepsilon_{km}}{\partial\overline{u}_{k\alpha}} = \frac{1}{2}E_{zykm}\left(\frac{\partial\phi_\alpha}{\partial x_m} + \delta_{mk}\frac{\partial\phi_\alpha}{\partial x_k}\right) = E_{zykm}\frac{\partial\phi_\alpha}{\partial x_m} \tag{22}$$

So far, the calculation of the implicit part of the total derivative of the von Mises stress w.r.t. $\widetilde{\rho}_{j,i}$ (19) has been presented. As regards the explicit part, one obtains:

$$\frac{\partial\sigma_e^{\mathrm{VM}}}{\partial\widetilde{\rho}_{j,i}} = \frac{\int_{\Omega_e^{\mathrm{d}}}\frac{1}{2}\left[\left(\frac{\partial\sigma_{11}^e}{\partial\widetilde{\rho}_{j,i}} - \frac{\partial\sigma_{22}^e}{\partial\widetilde{\rho}_{j,i}}\right)\left(\sigma_{11}^e - \sigma_{22}^e\right) + \frac{\partial\sigma_{11}^e}{\partial\widetilde{\rho}_{j,i}}\sigma_{11}^e + \frac{\partial\sigma_{22}^e}{\partial\widetilde{\rho}_{j,i}}\sigma_{22}^e + 6\frac{\partial\sigma_{12}^e}{\partial\widetilde{\rho}_{j,i}}\sigma_{12}^e\right]\mathrm{d}\Omega_e^{\mathrm{d}}}{\left|\Omega_e^{\mathrm{d}}\right|\sqrt{\frac{1}{2}\left[\left(\sigma_{11}^e - \sigma_{22}^e\right)^2 + \left(\sigma_{11}^e\right)^2 + \left(\sigma_{22}^e\right)^2\right] + 3\left(\sigma_{12}^e\right)^2}} \tag{23}$$

where the stress–strain relation (1) is here recalled to obtain the needed stress derivatives w.r.t. $\widetilde{\rho}_{j,i}$, which gives:

$$\frac{\partial\sigma_{zy}^e}{\partial\widetilde{\rho}_{j,i}} = \frac{\partial E_{zykm}}{\partial\widetilde{\rho}_{j,i}}\varepsilon_{km}\delta_{ie} \tag{24}$$

where $\boldsymbol{\delta}$ is the Kronecker delta. Here, the derivative of the stiffness tensor $\mathbf{E}$ simply involves the straightforward derivative of either (4) or (5), depending on the problem solved, MMTO or FGMTO, respectively.

3.3. Algorithm implementation

To solve problem (11) the authors pursued a Fortran programming implementation, which is schematically shown in Fig. 3. The algorithm starts by generating an initial design for the structure based on the two density design variables, ${}^0\boldsymbol{\rho}_1$ and ${}^0\boldsymbol{\rho}_2$. Filtered densities $\widetilde{\boldsymbol{\rho}}_1$ and $\widetilde{\boldsymbol{\rho}}_2$ are the input for FEM 2D [46]. Essentially, FEM 2D is a FE program that enables the solution of conventional plane elasticity problems using by default the 4-node quadrilateral isoparametric FE (Q4) along with the technique of Gaussian numerical integration, and it also postprocesses data to obtain strains and stresses. However, for the sake of quality approximations by FEM, the authors implemented the 8-node quadrilateral isoparametric FE (Q8), which avoids the shear-locking problem of Q4. Once the FEM 2D analysis is completed, convergence (e.g., iteration number, design change) is checked. In case convergence is verified, the algorithm stops. Otherwise, it continues iterating. The objective function f_0 and design constraints g_i values, and their respective derivatives, are then computed. The optimizer (MMA) updates the design variables, i.e., the non-filtered densities. So, sensitivities w.r.t. the non-filtered density design variables must be computed using the chain rule in (12). This process is called "Density filter grad" in the flowchart. Then, MMA updates $\boldsymbol{\rho}_1$ and $\boldsymbol{\rho}_2$. The density filter is applied before a new FEM 2D analysis is performed. This algorithm runs in loop until convergence is attained.

Sensitivity analysis is a well-known time-consuming task, especially when used to control stresses locally. To speed up the stress sensitivity analysis, the code is parallelized resorting to OpenMP directives [22] for Fortran. This requires parallelizing equation (19), which computes the total von Mises stress derivative at an element e w.r.t. $\widetilde{\rho}_{j,i}$, as detailed in Fig. 4. After inputting all the required data for the calculations, the parallel region is created using the directive !$OMP PARALLEL, where the public and private variables are defined. Two main loops are required to compute (19). An outer loop running through all stress constraints e, and an inner loop running through all density variables i. Since each stress derivative can be computed independently, i.e., the calculation of the derivative of one stress constraint has no impact on the calculation of the rest of the constraints derivatives, one parallelizes the outer loop using the directive !$OMP DO by appropriately distributing its iterations by different core processors (threads of the computer) with the SCHEDULE clause. This load balancing is done using the pre-defined ceiling function, i.e., $\lceil n_e/n_p \rceil$ where n_p is the total number of processors. Therefore, each processor runs the outer loop from $e = 1 + \lceil n_e/n_p \rceil \bullet \text{my\_ID}$ to $e = \lceil n_e/n_p \rceil \bullet (\text{my\_ID} + 1)$, where my_ID is the processor identification number. An adjoint problem (20) needs to be solved for each stress constraint e in order to compute the implicit and total stress derivatives w.r.t. all density variables $\widetilde{\rho}_{j,i}$. A speed-up curve is plotted in Fig. 5, where a quite good scalability is achieved for up to 16 cores.

4. Results

Several plane stress benchmarks are proposed here (see Table 1) to show the effectiveness of FGMs in stress mitigation in a range of typical loading scenarios, such as pure bending (Section 4.1), uniaxial-traction (Section 4.2), bulk (Section 4.3) and shear (Section 4.4) loading. All in-plane indicated dimensions are in meters and thickness is assumed

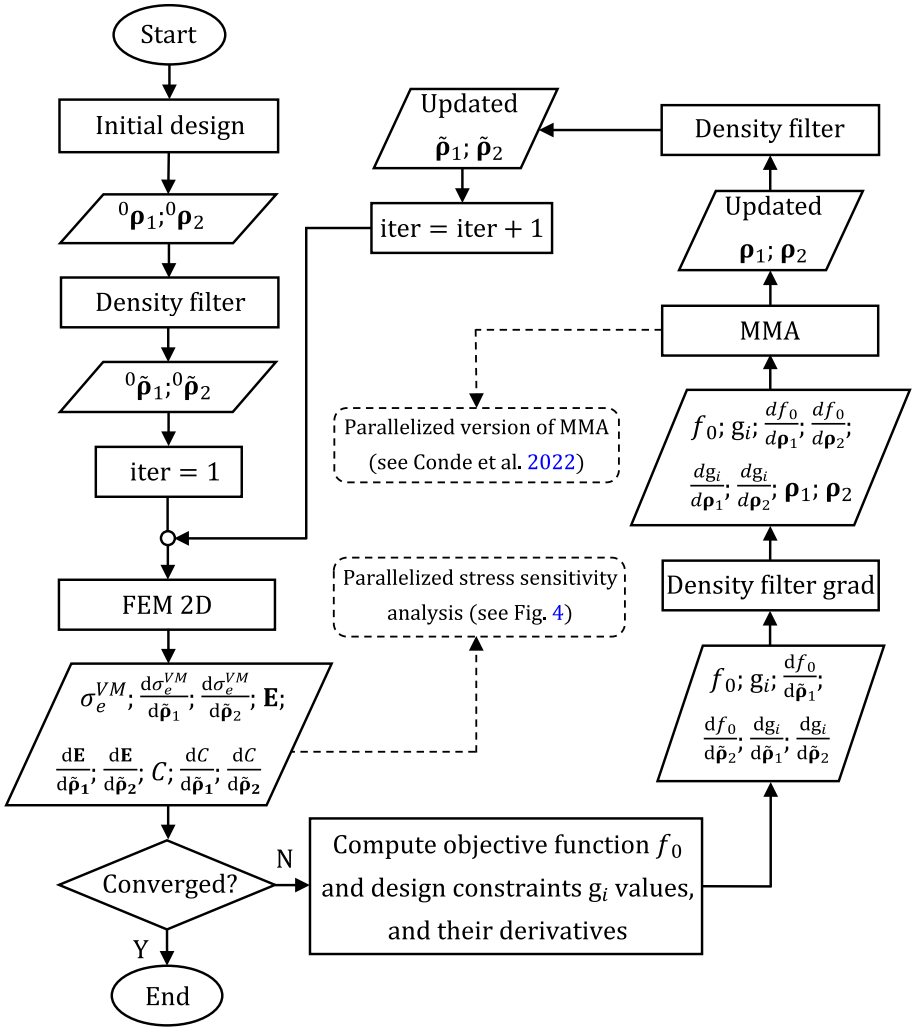

Fig. 3. Flowchart of the algorithm developed for the stress-based topology optimization in (11).

unitary to simplify. The FE models sketched in Table 1 (right), take advantage of the structures' symmetry and coarser meshes are shown to facilitate interpretation. The reduced models by virtue of symmetry require careful attention while implementing the density filter. The densities of the Q8 elements attached to the symmetry line are in fact mirrored. Hence, elements on both sides of such line must be included when averaging. Consistently, this also impacts on the sensitivity calculation through (12). Furthermore, the force-boundary conditions seen in Table 1 (FE model) are consistent with the intended externally distributed load (linear, hyperbolic, or uniform). The black and white meshed regions represent non-design areas in line with the material model representation used in Fig. 1.

Results are shown for SMTO, MMTO and FGMTO problems. SMTO and MMTO results are included to compare with FGMTO. For the sake of simplification and generalization of the results obtained, one conveniently normalizes material properties instead of using absolute values as problem input data. Therefore, defining the Young's Modulus E_1 of a selected reference material as unitary, 1 GPa, the value for the second material E_2 can also be interpreted as a property ratio. Below such ratio is inferior to 1, taken as 0.34 unless otherwise indicated in the examples. The Poisson's ratio is equal to 0.3. All stress results in this section are always to be read in MPa units.

Continuation approaches are used to improve convergence. The values of C^*, ζ_1 and ζ_2, see (11), gradually decrease over the course of the first design iterations, as explained below.

From the SMTO compliance minimization problem, it results a compliance value that is taken as reference to set a compliance upper bound C^* for the MMTO and FGMTO stress minimization problems. The C^* equals such reference value increased by a percentage, typically by 25% and 40% for the MMTO and FGMTO problems, respectively, as mentioned later in Sections 4.2 and 4.3. In Section 4.4, 20% and 35% are used instead. Depending on the problem solved, increasing C^* too much may lead to material connectivity issues. The C^* values are later presented in Section 5, for each example, and these are the end values as a continuation approach is used. Such approach relaxes well enough the compliance limit C^* in (11c) to ensure initial designs feasibility, and it gradually decreases it to the intended estimate of C^* based on the referred percentage. The number of iterations allotted to the continuation approach may depend on the problem solved. In the present framework, around 20 iterations work typically well. The beam examples in Section 4.1 have no need of the compliance constraint.

Regarding constraints (11e) and (11g), the ζ value must be tuned running the optimization a few times for each problem. In fact, a priori, without running any optimization, one does not know, at the optimum, the exact amount of "gray" that should only be remaining due to the density filter. Any meaningless gray that may come up is penalized by tightening bounds ζ and rerunning the optimization. Typically, an initial guess for ζ is a value high enough so that the respective constraint is nearly active. Then, by means of a continuation approach, one gradually decreases it to the intended ζ end value reported later in Section 5. The authors' acquired experience with these benchmarks is that the ζ

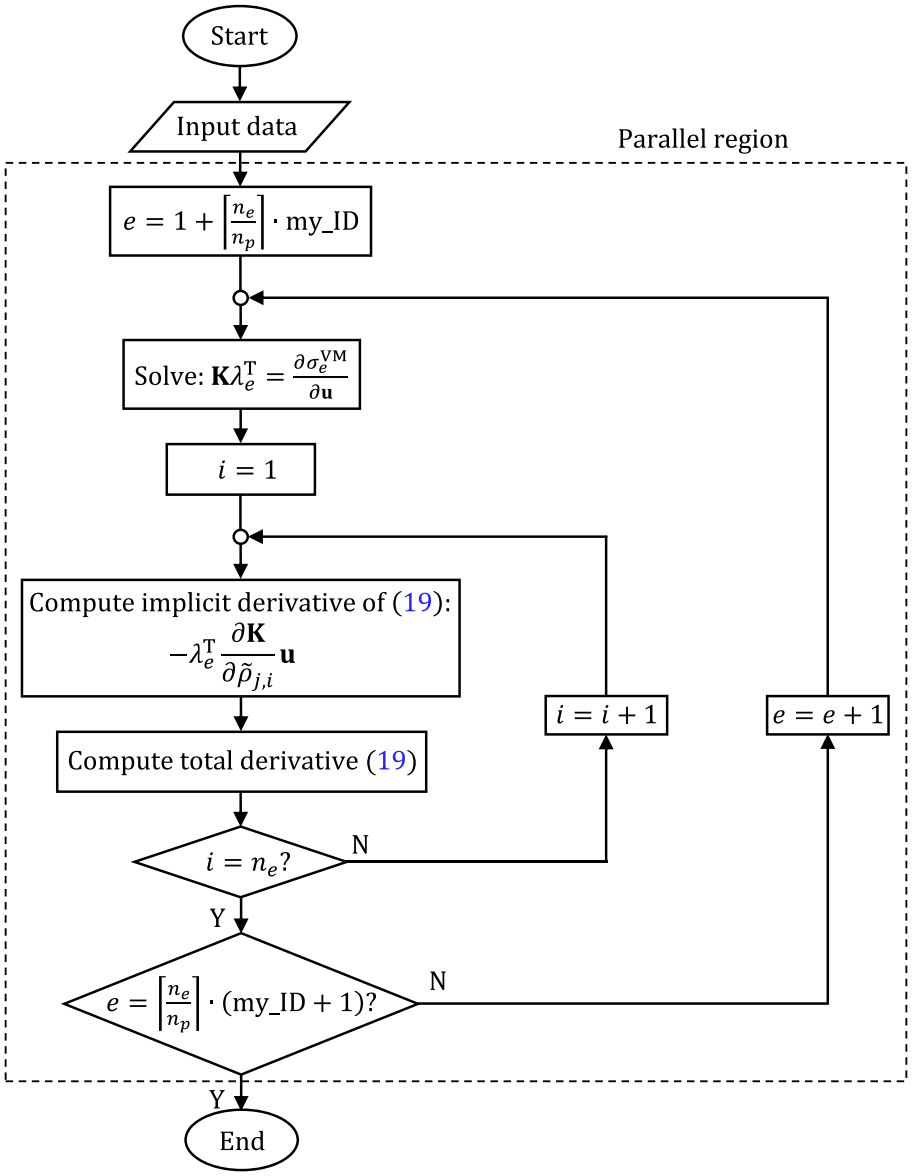

Fig. 4. Flowchart of the parallelized stress sensitivity analysis.

continuation approach must at least double the C^* continuation approach in terms of number of iterations.

The update of the design variable x must also be controlled by MMA to ensure small changes (jumps) of its value between iterations. From past authors' experience [15,17], unwanted x huge drops would otherwise be obtained, especially during the first iterations, leading to extensive violations on stress constraints, which would compromise algorithm's convergence. A high value chosen for the ALBEFA, parameter in the MMA Fortran code [81], allows having such needed control on x. Therefore, that ALBEFA is kept constant equal to 0.995 during the first 10 design iterations. Afterwards, one implements a continuation approach for that same ALBEFA along the next 15 design iterations such that its value linearly decreases from 0.995 to an end value of 0.5, which works fine. As regards the density variables update, the related ALBEFA remains constant equal to 0.1 (MMA default value).

As regards the compliance SMTO problem, needed to define the upper bound C^* in MMTO and FGMTO, one also applies a continuation approach to p_1, seen in (4) and (5), where it gradually increases during typically the first 40 design iterations.

Whenever appropriate in this section, both density fields, $\boldsymbol{\rho}_1$ and $\boldsymbol{\rho}_2$, are plotted next to each other to facilitate interpretation. However, recalling (4) and (5), it is noteworthy that the density field $\boldsymbol{\rho}_2$ is only meaningful in elements where $\boldsymbol{\rho}_1 = 1$. As regards the SMTO results, these are also obtained minimizing the maximum von Mises stress for the sake of consistency with the present paper focus, although the solution of the compliance minimization problem would be equivalent for the proposed benchmarks.

Next subsections detail how results were obtained for each benchmark. Then, next section discusses the variety of results obtained based on data collection and proper comparisons to draw conclusions.

4.1. Pure bending

A homogeneous straight beam under pure bending is an interesting starting point here since only normal stresses exist. Conceptually, material gradation between the beam's extreme fibers redistributes stresses, lowering them. Since all stresses are unidirectional (normal), the resulting FGM is also unidirectional (bottom-up), which possibly is the best proof-of-concept here due to its "simplicity". The work of Ituarte et al. [41] on FGM produced parts by multi-material additive manufacturing systems also starts by considering unidirectional gradation, but simply imposing it as linear, leaving behind any motivation

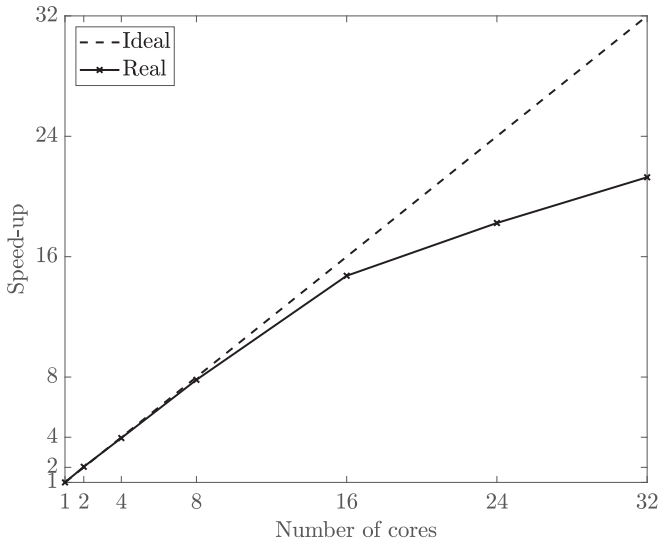

Fig. 5. Speed-up obtained in a problem with 7627 design variables and 3813 stress constraints.

from mechanics. In contrast, the unidirectional gradient considered here (although non-linear) is a result of optimizing a structure as simple as a beam under pure bending.

Two types of beams are studied, straight (Section 4.1.1) and curved (Section 4.1.2), see Table 1. TO of beams under pure bending is trivial because ideally a void is always inserted around and along the entire Neutral Surface (NS) length, but that compromises the structure connectivity. This motivates addressing here pure bending as a material optimization problem only – FGMO (Functionally Graded Material Optimization). This means that each point of the beam design domain is a material point (no void), and thus the problem only involves the pointwise selection of material. This variant of problem (11) simply means working only with design variables $_{\mathscr{x}}$ and $\boldsymbol{\rho}_2$ and only with stress constraints (11b). Note that the compliance constraint (11c) is no longer necessary, as there is no risk of structure absence or even loss of the structure's connectivity.

In the framework of the present paper, the straight beam example (Section 4.1.1) is selected to study the influence of possible different ratios $\widehat{r} = E_2/E_1$, see Table 2. Recall from Section 2 that the RAMP parameter q is material dependent, which means that it must be adjusted for the different ratios studied, as also summarized in Table 2.

4.1.1. Straight beam

In Table 1, the applied forces at the right end of the meshed beam, the real mesh has 100×50 elements, correspond to an applied bending moment M of 100 kN • m. This example results in optimal designs with no jagged boundaries and, taking into account that a higher-order element (Q8) is used, no checkerboard issues arise too. Therefore, the density filter is not used here. Moreover, the initial design corresponds to $\boldsymbol{\rho}_2 = 0.5$. Exact force-boundary conditions are used to render the linear stress distribution of pure bending on the predefined non-design area of the beam (where all $\rho_1 = \rho_2 = 1$), see the black region 4 in Table 1. In contrast, regions 1–3 of 3/4 in length correspond to the design domain (gray). Therefore, there is a transition zone between these design and non-design domains, typically zone 3, where a non-smooth variation (perturbation) of the stress field can be expected. Related stress peaks therein can easily unduly occupy the optimizer to render the FGM that best copes with such stress perturbations. However, the intended proof-of-concept in pure bending would be showing how ideally the FGM would deal with the original linear distribution of stresses. Such distribution only becomes steady far enough away from the discontinuity in the beam's cross-section found between regions 3 and 4 (Saint-Venant's principle). Therefore, the adopted strategy here is to minimize the maximum von Mises stress inside regions 1 and 2 only. However, one realizes that stress sensitivities w.r.t. densities consider that design variables embrace not only regions 1 and 2, but also region 3. The point is that stress control is shifted from regions 1–3 to regions 1–2 only avoiding the algorithm of being trapped in reducing stresses of the unwanted transition zone 3. Hence, the free design allowed in zone 3 is thus expected to promote stress uniformity in regions 1–2. Since the von Mises stress and densities are equal at opposite elements facing the NS, the number of design variables and stress constraints can be halved, as design variables are grouped in pairs. This simplification slightly changes the stress sensitivities computed through (19), in particular the derivative term of the global stiffness matrix w.r.t. density, because elements at opposite sides of the NS share the same density variable.

The analytical normal stress distribution for a homogeneous beam is given by $\sigma_{xx} = -My/I$, where $I = 1.042 \times 10^{-2}\,\mathrm{m}^4$ for this example. At extreme fibers this gives 2.40 MPa (modulus), numerically verified in the homogeneous zone 4 of the beam. The inhomogeneous zones 1–2, where an optimal FGM solution is investigated, present stress levels and distributions that differ depending on the property ratio $\widehat{r}$ considered, see Table 2. Fig. 6 shows the FGMO solutions with the corresponding density $\boldsymbol{\rho}_2$ and von Mises stress maps in every region. For each ratio, the stress peaks among all regions, and in region 1, are highlighted at the respective color scale. The FGM solution of interest is a layer-by-layer gradation of properties (layer-wise FGM), having each layer constant stress, and stress uniformity is obtained across several layers, as seen in regions 1 and 2. However, stress in region 2 may still appear perturbed, as region 3 may not fully absorb the cross-section discontinuity effects. Therefore, the desired FGM is purely obtained in region 1. Since there is no limit on compliance, no matter how low or high the material ratios considered are, the FGM fully exploits the range of properties possible between the weak and strong phases selected. Furthermore, the higher the ratio, the smaller the gradation area. In the limit, as $\widehat{r} \to 1$, a homogeneous beam is attained. On the contrary, as $\widehat{r} \to 0$, one gets more FGM and lesser peak stresses, but a fully stressed design can't be attained as stresses will always vanish at the NS.

4.1.2. Curved beam

Consider an applied bending moment of 10 kN • m and half of the beam modelled with 100×50 elements generated at different radius and angles, adapted to the curved beam geometry, see Table 1. No filtering is used, and the initial design is $\boldsymbol{\rho}_2 = 0.5$ everywhere.

The circumferential stress distribution for the curved beam is hyperbolic given by $\sigma_{\theta\theta} = -M(R-r)/Aer$, where r locates the beam fiber, A is the cross-section area, $e = \bar{r} - R$ where radius $\bar{r}$ locates the cross-section centroid, radius $R = h/\ln(R_2/R_1)$ locates the NS, assuming a rectangular cross-section with height h, and R_1 and R_2 are the inner and outer radius of the curved beam, respectively, see Table 1. However, the above curved beam formula for circumferential stress is based on the assumption that the effect of radial stress is small, which is quite accurate here since one assumes a rectangular cross-section. Furthermore, the NS and beam centroid are not coincident ($e \neq 0$) in this case, requiring that one keeps design variables on both sides of the NS, unlike the straight beam. At inner and outer fibers, the analytical circumferential stress is 1.06 MPa and 0.88 MPa (in modulus), respectively. These values were verified at the inner and outer fibers, respectively, by the numerical model at the non-designable region 4, see Table 1, keeping the beam divided in four regions as done for the straight beam. Therefore, stresses are only minimized in regions 1 and 2.

The FGMO result is presented in Fig. 7 considering now only one ratio, $\widehat{r}_2$. Material gradation is obtained layer-by-layer (concentric layers), but different at opposite sides of the NS, as $e \neq 0$. In Fig. 7 (right), $\boldsymbol{\rho}_2$ is plotted alone to clearly show material uniformity along the circumferential direction and property changes (FGM) along the radial direction. The Young's Modulus range with ratio $\widehat{r}_2$ is fully used to

Table 1
Benchmarks selected according to different loading types and the respective FE models.

Loading-type	Benchmark	FE Model
Pure Bending	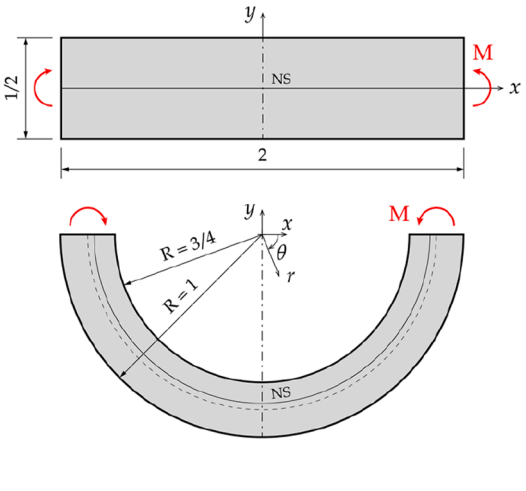	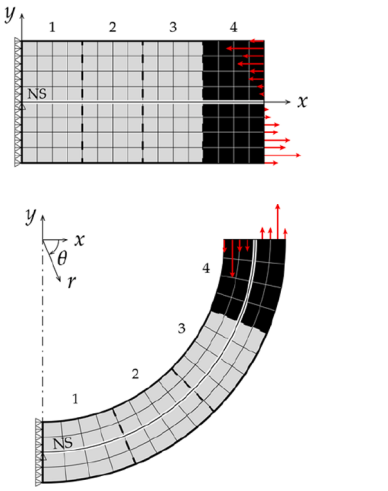
Uniaxial	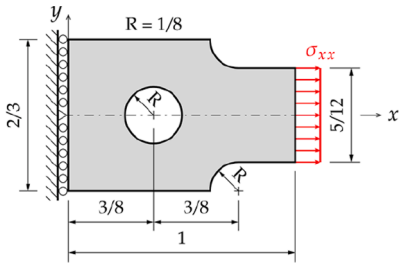	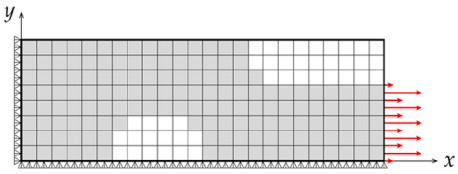
Bulk	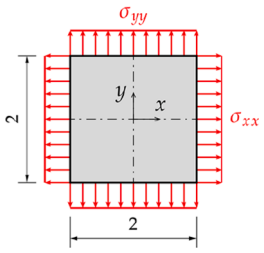	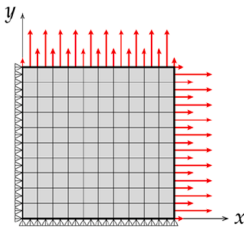
Shear	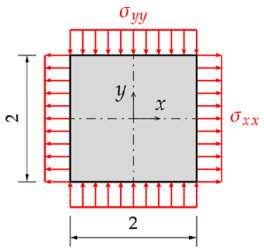	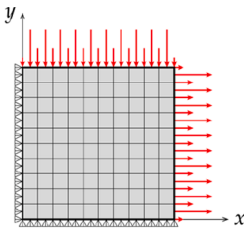

Table 2
Different material property ratios $\hat{r}$ considered for the straight beam example and respective RAMP parameter q values.

Ratios $\hat{r} = E_2/E_1$	RAMP parameter (q)
$\hat{r}_1 = 0.10$	3.75
$\hat{r}_2 = 0.34$	1.04
$\hat{r}_3 = 0.67$	0.305

define the FGM as no limit on compliance is imposed. An almost fully stressed design is obtained to reduce the original peak stress from the hyperbolic distribution.

4.2. Uniaxial-traction

From now onwards, one solves the design problems with both topology changes and material selection. To study the interest of FGM solutions for structures under uniaxial-traction, one selects here the link-bar example [47], see Table 1. A constant pressure of 1 MPa is applied at the right end. The volume fraction limit V^* within the design domain (colored as gray) is set to 80%, allowing for additional hole openings that help redistributing stresses even more evenly as shown below. Notice that two non-design domains are defined in Table 1, the blank areas: hole and fillet. The FE model, with 120×40 elements, is half of the structure due to symmetry. Initial uniform distribution of $\boldsymbol{\rho}_1 = 0.8$ is considered. As regards the initialization of $\boldsymbol{\rho}_2$, for MMTO one defines a homogeneous domain with two rectangular inclusions of low density,

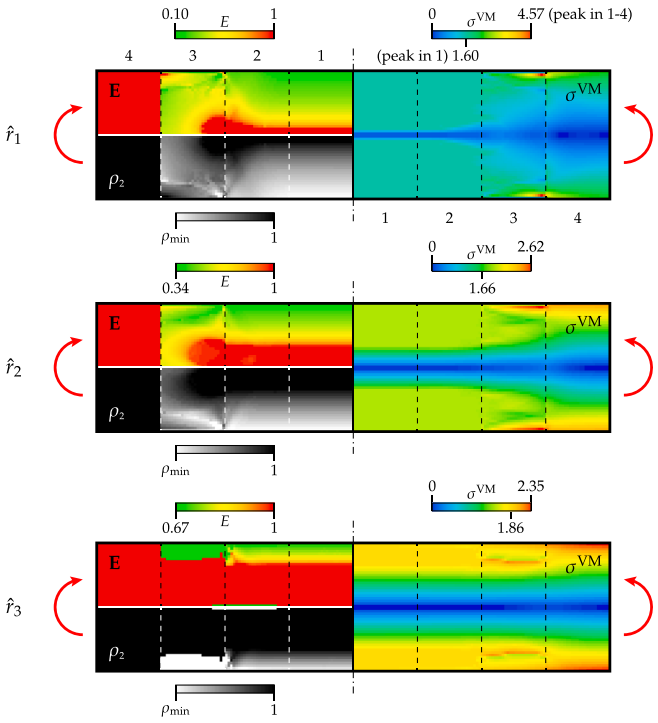

Fig. 6. Material selection (FGMO) results for the straight beam. Young's Modulus, density and stress maps. The peak stresses obtained among all regions, as well as in region 1 only, are highlighted at the color scale.

one located next to the central hole on the left and the other at the lower right-side corner of the FE model. For FGMTO, one has $\boldsymbol{\rho}_2 = 0.5$ everywhere.

The SMTO, MMTO and FGMTO results are present in Fig. 8. For SMTO, one solves (11) excluding (11e), the corresponding stress map evidences a couple of stress peaks highly localized. The MMTO result shows comparatively an interesting stress improvement. In this case, a more compliant solid appears (see green) at the expense of increasing compliance by 25% through C^* in (11c). Although compliance is allowed to increase, it is still low enough to prevent connectivity losses or no structure. In MMTO here, p_1 and p_2 in (4) remain constant equal to 4 along iterations. These penalizations of intermediate densities are not enough and thus further penalizations through constraints (11e) and (11g) are carried out for the sake of well-defined discrete solid phases. The bounds ζ_1 and ζ_2 need to be properly adjusted, their final values are presented later in Section 5. The presence of the weak solid is imposed through the volume fraction constraint (11f), at least 10% ($V_2 \geq V_2^* = 0.1$).

The FGMTO result is shown in Fig. 8 (right). In this case, the compliance is worsened by 40%, being (11c) active at optimum, comparing to the minimum compliance from SMTO. The interpolation scheme (5) is used with penalization parameters p_1 and q constant and equal to 4 and 1.04, respectively, see Section 2. The intermediate values of $\boldsymbol{\rho}_1$ are stirred to 0 and 1 through (11e), while the intermediate values of $\boldsymbol{\rho}_2$ define an FGM. The resulting optimal material distribution approximates a fully stressed design associated with lower stress levels, see Fig. 8 (right). Finally, as an example of the optimization history, Fig. 9 shows the evolution of the objective function and the variations in constraints violation along the design iterations of the FGMTO problem.

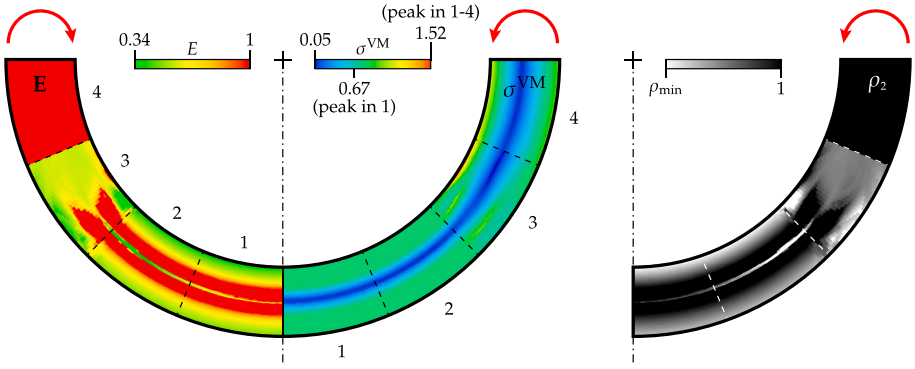

Fig. 7. FGMO result for the curved beam.

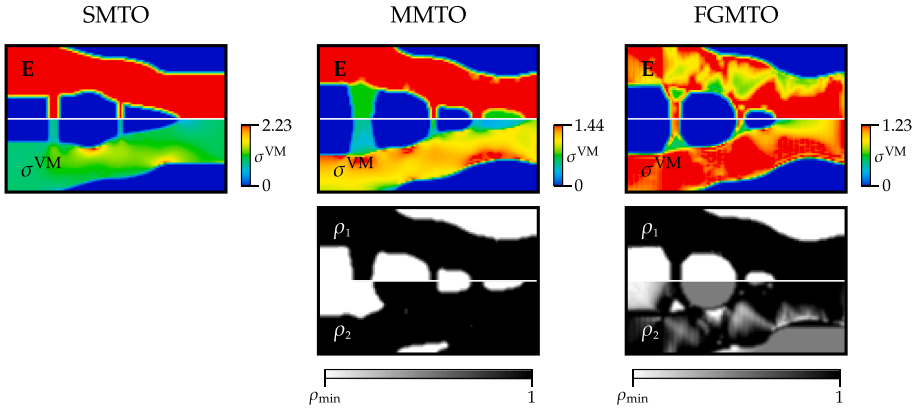

Fig. 8. Link-bar results obtained from SMTO (left), MMTO (center) and FGMTO (right).

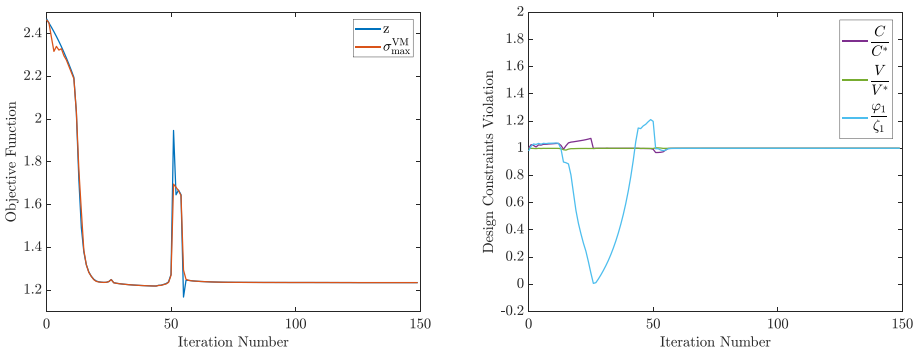

Fig. 9. Optimization history of the stress-based FGMTO problem considering the uniaxial-traction load.

4.3. Bulk-type load

Consider a square plate under plane stress with $\sigma_{xx} = \sigma_{yy} = 1$ MPa (bulk-type load). A volume fraction upper bound V^* of 90% is used. Different initial designs are used depending on the optimization problem solved. Regarding SMTO, only $\boldsymbol{\rho}_1$ exists and the related plate initial design is a centered circle of lower uniform density surrounded by uniform density distribution of higher value. Regarding MMTO and FGMTO, $\boldsymbol{\rho}_1$ and $\boldsymbol{\rho}_2$ need to be initialized. In the case of $\boldsymbol{\rho}_1$, round inclusions of uniform lower density are generated, a circle at plate center and a quarter-circle centered at each plate corner. In the case of $\boldsymbol{\rho}_2$, and MMTO, one generates semi-circles of uniform lower density centered at midpoints of each plate edge. For FGMTO, $\boldsymbol{\rho}_2$ is uniform, equal to 0.5. However, this must be adapted as the full plate is not modelled, but only a quarter (using 50×50 FEs), taking advantage of symmetry.

The stress-based SMTO design solution is a perforated homogeneous plate (assuming $E = 1$ GPa), see Fig. 10 (left) where a quarter is represented. In theory, a plate weakened by a hole, considering the plate infinite or the hole infinitesimal, under the same bulk load, has a stress concentration factor of $K_t = 2$ (see Young et al. [93]). However, these theoretical assumptions are not verified in the present plate. Therefore, the obtained maximum stress is slightly higher than 2 MPa. Anyway, this stress distribution verifies the Equi-Stress Principle [14] as expected, and resembles the results obtained by Coelho et al. [15] in the framework of stress-based microstructural TO.

The MMTO design solution presented in Fig. 10 (center) contains 10% (the minimum allowed) of the second material (softer), worsening the compliance by 25% (comparing to SMTO), similarly to what was done in Section 4.2. Interestingly, the multi-material layout found shows a second hole (smaller) close to the plate corner, which is a significant finding as it recovers hole openings as a standard design procedure to mitigate stress concentrations. Therefore, the addition of both softer material and hole reduce considerably the peak stress. Yet, room is left for further stress reduction on account of FGMTO that results in stresses more evenly distributed, see now Fig. 10 (right). To that purpose, the compliance is further worsened, by 40%, comparing to SMTO. The gradient of properties obtained is obviously visible in a large area of the plate causing a quite uniform distribution of von Mises stress in the full plate.

4.4. Shear-type load

Consider a square plate under plane stress with $\sigma_{xx} = 1$ MPa and $\sigma_{yy} = -1$ MPa (shear-type load). A volume fraction upper bound V^* of 90% is used. For the initial design of $\boldsymbol{\rho}_1$, one considers a square inclusion of low density located at the plate center, followed by both horizontal and vertical parallel slots of low density as one moves towards the plate border. Regarding the MMTO case, the initial design of $\boldsymbol{\rho}_2$ features inclusions of low density, located at the sharp corners of the central square inclusion and at the plate corners. In the FGMTO case, the initial design is defined by setting $\boldsymbol{\rho}_2$ equal to 0.5. Bear in mind that only a quarter of the plate is meshed, taking advantage of symmetry, with 50×50 elements.

The SMTO result is presented in Fig. 11 (left). The optimal layout found here exhibits a central square-like hole, with slots parallel to the edges of the hole. In the compliance minimization setting, a continuation approach such that $p_1 = 2 \rightarrow 10$ (during the first 80 iterations) is applied in order to obtain a clear "black-white" design. The same p_1 value is therefore used in the stress-based SMTO problem.

In MMTO, the compliance is worsened by 20% comparing to the SMTO counterpart. Once again, at least 10% of solid $\mathbf{E}_2$ is enforced. The penalization exponents p_1 and p_2 in (4) are equal to 4 in the MMTO setting as one uses constraints (11e) and (11g) to further penalize intermediate densities with no physical meaning. The parallel slots

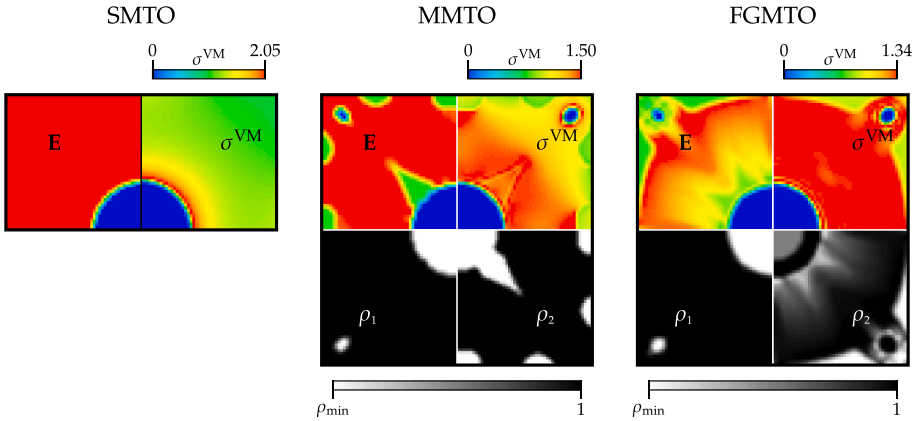

Fig. 10. Stress-based SMTO (left), MMTO (center) and FGMTO (right) results for the bulk-type load case.

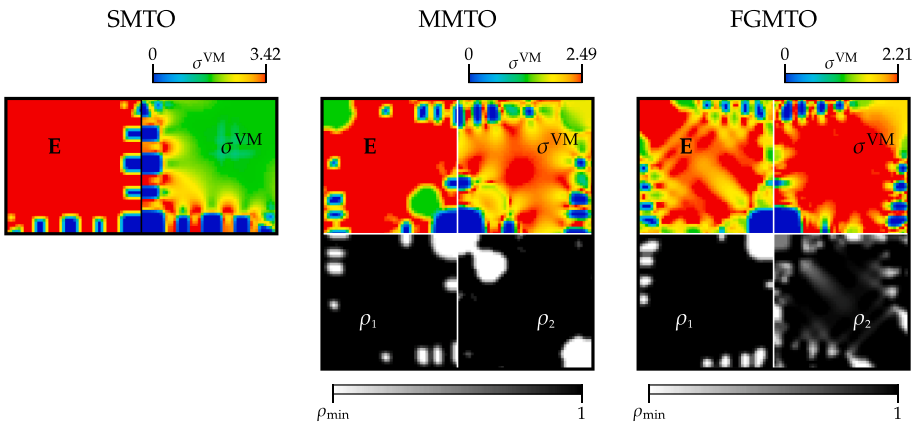

Fig. 11. Optimal designs obtained for the stress-based SMTO (left), MMTO (center) and FGMTO (right) problems considering the shear-type load.

previously identified are now located near the edges of the plate, see Fig. 11 (center). The softer phase around the sharp corners of the center hole and at the plate corners now can lower the initial peak stresses, as new stress peaks appear of lower magnitude. In FGMTO, the compliance is increased by 35% compared to SMTO. The penalization parameters p_1 and q in (5) are set to 4 and 1.04, respectively. The stress plot in Fig. 11 (right) shows basically a large solid area experiencing the same stress level. Unlike the microstructural results for the same volume fraction, shown by Coelho et al. [15], significant stress reductions are obtained here in both MMTO and FGMTO cases for the shear loading problem, which will be summarized later in Section 5.

5. Discussion

Based on the data of the previous section, one discusses how multi-material design solutions, especially FGMs, outperform conventional (single-material) ones. Firstly, one discusses the beam examples, straight and curved geometries under pure bending. Then, one discusses the remaining benchmark results previously presented.

Table 3 compares compliance C and stress σ values between the homogeneous and graded material beam design solutions, for straight and curved geometries. As the multi-material solution is comparatively inefficient in reducing the maximum stress, as noticed by the authors, it is skipped here. The stress distribution is material-independent for the homogeneous beam, unlike compliance. The homogeneous beam of stiff material has compliance C_1, whereas C_2 is when only weak material exists. The compliance is computed considering region 1 only, as it is where a well-defined FGM (unidirectional/radial) is caught and responsible for converting the original (linear/hyperbolic) stress distribution into a more uniform one. Although the beams' FGMO problem is compliance-free, one measures it, and it falls within the interval $[C_1, C_2]$. Hence, the FGM solution increases or decreases compliance depending on the reference material set for the homogeneous beam. The percentages shown in Table 3, see δ_{FGMO}, indicate that the FGM beams, when compared to the homogeneous counterparts, are much more compliant (choosing E_1 as reference) than stiffer (choosing E_2 as reference). However, as stress is the problem objective function, FGM design solutions are always considerably less stressed (roughly 30% less) than the homogenous solutions. In fact, as shown through the straight beam example, the benefits on stresses also depend on the property ratio $\widehat{r}$ considered, noticing that lower ratios ($\widehat{r}_3 \rightarrow \widehat{r}_1$) mean wider gradation zones which reduce stresses even further.

Table 3
Compliance [J] and peak stress [MPa] values for both straight and curved beams. Three material ratios are studied for the straight beam example.

		Straight beam			Curved beam
		$\widehat{r}_1$	$\widehat{r}_2$	$\widehat{r}_3$	$\widehat{r}_2$
Single-Material (SM)	C_1	120	120	120	13
	C_2	1200	360	180	39
	σ^{VM}_{max}	2.40	2.40	2.40	1.06
FGMO	C	817	249	142	24
	σ^{VM}_{max}	1.60	1.66	1.86	0.67
$\delta_{FGMO}(\%)$	C_1	**+580.8**	**+107.5**	**+18.3**	**+84.6**
	C_2	**−31.9**	**−30.8**	**−21.1**	**−38.5**
	$\sigma^{VM}_{max,SM}$	**−33.3**	**−30.8**	**−22.5**	**−36.8**

The chart in Fig. 12 (left) has two data sets for each material ratio $\widehat{r}$ studied in the straight beam example. Recall the beam coordinate system given in Table 1 and that only half of the beam (say above NS line) is informative enough. One plot is the material gradation curve, i.e., the variation of E along y-axis. Every FGM solution fully covers the span of properties allowed by each ratio considered. Another plot is the distribution of von Mises stress. Cleary, many fibers are saturated with uniform maximum stress, those within the FGM region of influence. Such region enlarges as $\widehat{r}$ decreases, leading to lower levels of maximum stress. For $\widehat{r} = 0.1$, a stress plateau is almost attained across the entire beam's height, realizing that stress always vanishes at NS. The chart in Fig. 12 (right) is of the same type as just discussed, but applied to the curved beam where only $\widehat{r} = 0.34$ is studied. The full beam height is represented as no symmetry applies. Therefore, the material gradation above and below the NS line differs as well as the stress distribution. Noteworthy is the fact that von Mises stresses coincide with normal stresses in the straight beam case, but for the curved one they only coincide with circumferential stresses (normal to the cross-section) at the extreme fibers because, apart from those fibers, radial stresses also exist in this latter case. This explains why von Mises stresses do not vanish at the NS, as seen in Fig. 12 (right). Anyway, an interesting stress plateau is attained reducing the original stress peak by 37%, as indicated in Table 3.

Curve fitting can be used based on the set of points obtained for Young's Modulus in the FGM region of influence in both straight and curved beams. According to the literature, it is common to find studies on FGM beams in which the material distribution is given by a power-law [8,2]. The curve fitting here is also based on power-laws, $E(t) = at^b + c$, with the coefficient values presented in Table 4, which perfectly match the trends predicted by the numerical simulations. The range of admissible values for t, with $t \in [d; e]$, is provided as well to account for the FGM region of influence in both straight and curved beams.

Unlike the beam examples, the examples of Sections 4.2 to 4.4 are used to find out, not only the optimal material selection, but also the optimal topology (FGMTO problem). Table 5 summarizes the compliance, mass, ζ_1, ζ_2, and peak stress values to compare results among the SMTO, MMTO and FGMTO problems. The mass calculations for the FGMTO solutions simply assume a linear interpolation between mass

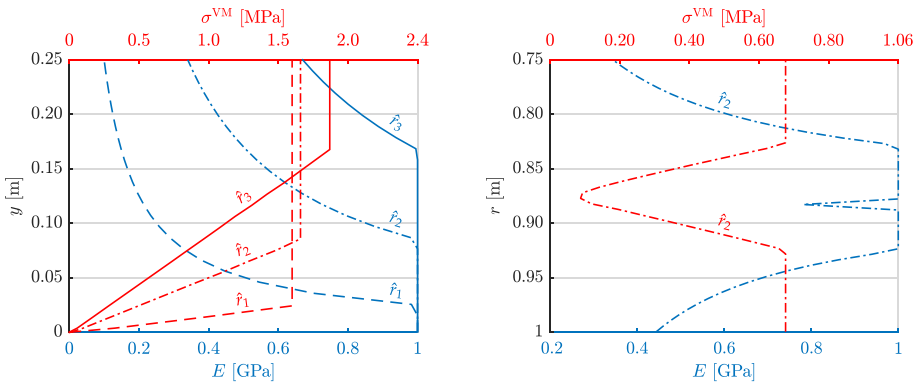

Fig. 12. Young's Modulus distribution and stress distribution for the straight beam (left) and curved beam (right).

Table 4
Power-laws for the Young's Modulus distribution in the FGM region of influence obtained by curve fitting for both straight and curved beams.

Beam type		Ratio	$E(t) = at^b + c$			R^2	$t \in [d; e]$	
			a	b	c		d	e
Straight ($t \equiv y$)	Above NS	$\hat{r}_1$	0.0251	−1	0	1	0.0251	0.25
		$\hat{r}_2$	0.0851				0.0851	
		$\hat{r}_3$	0.1676				0.1676	
Curved ($t \equiv r$)	Above NS	$\hat{r}_2$	38.850	21.05	0.2560	1	0.75	0.8287
	Below NS		0.1184	–23.10	0.3342		0.9244	1

Table 5
Compliance [J], mass [kg], and peak stress [MPa] values for stress-based FGMTO compared to SMTO and MMTO.

		Uniaxial	Bulk	Shear
SMTO	C_1	125	949	1935
	C_2	368	2792	5690
	m_1	0.212	$\equiv V^*$	$\equiv V^*$
	m_2	0.072	0.306	0.306
	σ^{VM}_{max}	2.23	2.05	3.42
MMTO	C	143	1184	2223
	m	0.194	0.834	0.834
	σ^{VM}_{max}	1.44	1.50	2.49
	ζ_1	80	18	60
	ζ_2	110	48	40
δ_{MMTO}(%)	C_1	**+14.4**	**+24.8**	**+14.9**
	C_2	**−61.1**	**−57.6**	**−60.9**
	m_1	**−8.5**	**−7.3**	**−7.3**
	m_2	**+169.4**	**+172.5**	**+172.5**
	$\sigma^{VM}_{max,SMTO}$	**−35.4**	**−26.8**	**−27.2**
FGMTO	C	175	1329	2611
	m	0.188	0.756	0.812
	σ^{VM}_{max}	1.23	1.34	2.21
	ζ_1	80	20	64
δ_{FGMTO}(%)	C_1	**+40**	**+40**	**+35**
	C_2	**−52.4**	**−52.4**	**−54.1**
	m_1	**−11.3**	**−16**	**−9.8**
	m_2	**+161.1**	**+147.1**	**+165.4**
	m_{MMTO}	**−3.1**	**−9.4**	**−2.6**
	$\sigma^{VM}_{max,SMTO}$	**−44.8**	**−34.6**	**−35.4**
	$\sigma^{VM}_{max,MMTO}$	**−14.6**	**−10.7**	**−11.3**

densities of the two base materials. The ratio of these mass densities equals here the Young's Modulus ratio (0.34), which is valid for engineering alloys [3]. In the SMTO case, two compliance (C_1, C_2) and mass (m_1, m_2) values of reference are shown, as the same stress field is obtained on homogeneous solutions considering either the stiff (E_1) or weak (E_2) solid as base material. The δ_{MMTO} in Table 5 shows in percentage how much more (or less) compliant or lightweight the MMTO designs are compared to SMTO designs, depending on the single-material chosen as reference. Anyway, stresses are always lower in multi-material solutions. The percentage δ_{FGMTO} does the same comparative analyses, but comparing FGMTO to MMTO and SMTO. Therefore, concerning the compliance constraint (11c), if C^* is below the minimum compliance found in SMTO using the weak solid as base material, advantages in terms of stiffness are obtained in both MMTO and FGMTO problems. If one sets C^* above the minimum compliance found in SMTO using the stiff solid as base material, a more compliant design is obtained in the multi-material setting.

The results of MMTO designs in Table 5 demonstrate their superior strength (lower stress levels) compared to SMTO designs. The stress FGMTO results are even superior to MMTO, being even comparatively lighter. The stress distribution plots in Figs. 8, 10 and 11 (right side) highlight how the FGMTO solution outshines the other two, SMTO and MMTO, as it exhibits a significantly more uniform stress field.

The von Mises stress values behind the color maps shown in Figs. 8, 10 and 11 are collected and displayed in Fig. 13 to better compare the continuous variation of stresses among the SMTO, MMTO and FGMTO results. All the FEs with the selected stresses plotted in Fig. 13 were listed and reordered in ascending order $N_s = 1, \cdots, N_{max}$, and normalized by the total number of plotted elements, N_{max}, see the abscissa axis. The selected stress values σ^{VM}_s, with $s \in \{1, \cdots, N_{max}\}$, are also normalized by the maximum stress value obtained in SMTO, $\sigma^{VM}_{max,\,SMTO}$, see the ordinate axis. Basically, a minimum stress threshold is defined, say 10^4, above which von Mises stresses are plotted in Fig. 13. To sum up, the SMTO stress curve clearly escalates; the MMTO curve increases at moderate slope; and the FGMTO curve is comparatively quite flat for a wide range of elements, which plainly highlights the FGM efficiency on attaining

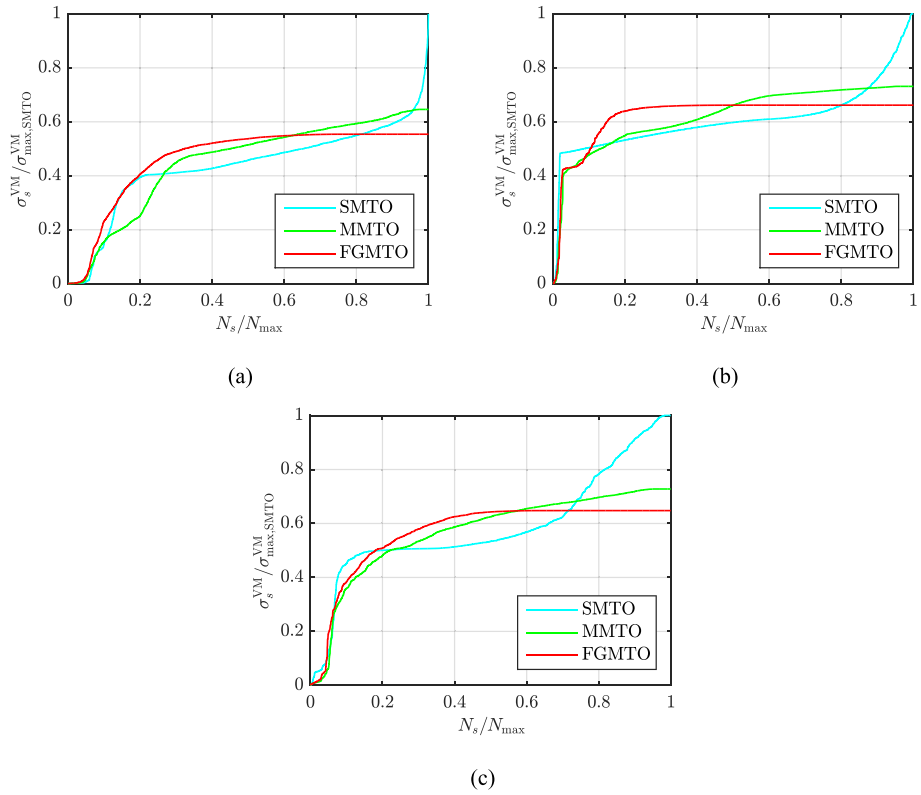

Fig. 13. Stress distributions obtained from SMTO, MMTO and FGMTO problems are compared considering the following loading-types: (a) uniaxial-traction, (b) bulk, and (c) shear.

uniform stress distributions.

6. Conclusions

Stress concentrations in structural parts are a common concern in engineering practice and that is why structural design engineers work on solutions to mitigate them. At a conceptual design stage, TO plays a very important role and thus may give a valuable insight about form finding, as well as multi-material best distributions to minimize stress problems.

Major research in the field of strength-oriented TO has focused on volume (weight) or compliance minimization under stress constraints. Undoubtedly, that is a problem formulation of great practical interest as it assures that the failure stress is not exceeded in any of the design materials. However, the topology design problem can be conveniently reformulated to define stress as the objective to be minimized while volume and compliance are constrained, as addressed here. This TO problem formulation is not that much covered in the literature. The interest in such formulation can be leveraged by considering multi-material design solutions. As a first approach, if one expands the design space to capture FGM solutions, it can be more challenging to do it by imposing an allowable stress due to the lack of consistent reported predictions on the FGM yielding stress. In fact, the material's continuous variation in composition brings challenges to assess the resulting material properties. As regards the Young's Modulus variation, theoretical interpolations exist based on the HS bounds and they have been consistently used when experimental data is not available. Therefore, the present work on strength-oriented design calculates the von Mises stress to handle it as a design objective (to be minimized) rather than constraining it to an allowable stress. Actually, this is a problem formulation that is even more appropriate to exploit the stress mitigation potential of FGMs as aimed here on account of optimal design of material composition distribution. For that purpose, it is proposed a material model (SIMP-RAMP) that, besides identifying topology, also maps the volume fraction of materials mixtures into the constitutive tensor of the resulting composite material based on the HS bounds. For comparison purposes, the present work also applies TO to the design of classical composites, i.e., characterized by discrete material phases separated by sharp interfaces. For demonstration purposes, the stress-based formulation (11) is applied to 2D structures, as beams and plates with force/displacement-based boundary conditions. Different load cases are explored as pure bending, uniaxial-traction, bulk, and shear-type loads.

In the context of material selection only (straight beam example), the impact of different material ratios is investigated, aiming to understand how the properties of the base materials influence the FGM generation and the related stress reduction. A higher difference between the Young's Modulus of the base materials leads to lower peak stresses. From a materials science perspective, the absolute moduli, or the individual materials, is a non-trivial choice as physical limitations exist as regards materials mixtures, especially for metals. One tries to avoid here this kind of issue by working with ratios, although too low (or too large) ratios can also become an issue. Leaving the ratio viability aside, the proof-of-concept established here is that the FGMTO problem formulation leads to a significant stress reduction for all load types covered. As seen in the examples chosen, FGM effectiveness in stress mitigation comes along with higher volume fractions. In fact, "truss-like" solutions, obtained from imposing lower limits on volume fractions, tend *per se* to render less continuous stress gradients favoring more the discrete distribution of material phases rather than their mixture to generate an FGM. This is an aspect observed by the authors while searching for benchmarks. Furthermore, a concentrated applied force generates a stress singularity that absorbs the FGM solution in the way that its zone of influence becomes much more localized rather than continuous. This kind of stress concentration is not realistic and should be avoided by applying distributed loads. Anyway, more localized loads mean more localized FGMs. For the sake of demonstration purposes on FGM

effectiveness in reducing stresses, the chosen examples have external applied loads quite distributed.

In the present work two important bottlenecks exist as stresses are computed and controlled in many FEs, i.e., the sensitivity analysis and the optimizer (MMA). As regards the MMA, important speedups are attained here by resorting to the parallelized version of MMA as developed by Conde et al. [17]. As regards the sensitivity analysis, the stress derivative (19) is parallelized using the OpenMP directives.

As future work the authors may anticipate several possible trends: (1) extending the proposed approach to the thermoelasticity problem, since a direct treatment of thermal stresses is not well documented; (2) saving computational time by working on an alternative formulation of the min–max problem; (3) applying other TO approaches, besides density-based approaches, to the same problem proposed here (e.g., the Level-set method, [87]); (4) investigate on multi-material additive manufacturing systems to generate FGM-like solutions.

CRediT authorship contribution statement

Rui F. Silva: Writing – review & editing, Writing – original draft, Visualization, Software, Methodology, Investigation, Formal analysis. **Pedro G. Coelho:** Writing – review & editing, Writing – original draft, Supervision, Resources, Project administration, Funding acquisition, Formal analysis, Conceptualization. **Fábio M. Conde:** . **Bernardo R. Santos:** Visualization, Software, Investigation. **João P. Oliveira:** Writing – review & editing.

Declaration of competing interest

The authors declare that they have no known competing financial interests or personal relationships that could have appeared to influence the work reported in this paper.

Data availability

Data will be made available on request.

Acknowledgements

The authors acknowledge funding by national funds from FCT - Fundação para a Ciência e a Tecnologia, I.P., in the scope of the following projects: 2022.06903.PTDC - TOP&AM4FGM (http://doi.org/10.54499/2022.06903.PTDC); UIDB/00667/2020 and UIDP/00667/2020 (UNIDEMI); IDMEC, under LAETA, project UIDB/50022/2020; LA/P/0037/2020, UIDP/50025/2020 and UIDB/50025/2020 of the Associate Laboratory Institute of Nanostructures, Nanomodelling and Nanofabrication – i3N. The authors wish also to thank Professor Krister Svanberg (Royal Institute of Technology, Stockholm, Sweden) for the MMA optimization code and Professor Noboru Kikuchi (University of Michigan, USA) for the FEM 2D Fortran code.

References

[1] Alacoque L, Watkins RT, Tamijani AY. Stress-based and robust topology optimization for thermoelastic multi-material periodic microstructures. Comput Methods Appl Mech Eng 2021;379:113749. https://doi.org/10.1016/j.cma.2021.113749.
[2] Althoey F, Ali E. A simplified stress analysis of functionally graded beams and influence of material function on deflection. Appl Sci 2021;11(24):11747. https://doi.org/10.3390/app112411747.
[3] Ashby M. Materials selection in mechanical design. 2nd Ed. Butterworth Heinemann; 1999.
[4] Bendsøe MP, Kikuchi N. Generating optimal topologies in structural design using a homogenization method. Comput Methods Appl Mech Eng 1988;71:197–224. https://doi.org/10.1016/0045-7825(88)90086-2.
[5] Bendsøe MP. Optimal shape design as a material distribution problem. Struct Optim 1989;1(4):193–202. https://doi.org/10.1007/BF01650949.
[6] Bendsøe MP, Sigmund O. Material interpolation schemes in topology optimization. Arch Appl Mech 1999;69:635–54. https://doi.org/10.1007/s004190050248.
[7] Bendsøe MP, Sigmund O. Topology optimization: theory, methods and applications. Berlin: Springer; 2004.
[8] Birman V, Byrd LW. Modeling and analysis of functionally graded materials and structures. Appl Mech Rev 2007;60(5):195–216. https://doi.org/10.1115/1.2777164.
[9] Bruggi M. On an alternative approach to stress constraints relaxation in topology optimization. Struct Multidiscip Optim 2008;36(2):125–41. https://doi.org/10.1007/s00158-007-0203-6.
[10] Bruggi M, Duysinx P. Topology optimization for minimum weight with compliance and stress constraints. Struct Multidiscip Optim 2012;46:369–84. https://doi.org/10.1007/s00158-012-0759-7.
[11] Bruns T, Tortorelli D. Topology optimization of non-linear elastic structures and compliant mechanisms. Comput Methods Appl Mech Eng 2001;190(26–27):3443–59. https://doi.org/10.1016/S0045-7825(00)00278-4.
[12] Bruyneel M, Duysinx P. Note on topology optimization of continuum structures including self-weight. Struct Multidiscip Optim 2005;29(4):245–6. https://doi.org/10.1007/s00158-004-0484-y.
[13] Cheng GD, Guo X. ε-relaxed approach in structural topology optimization. Struct Optim 1997;13:258–66. https://doi.org/10.1007/BF01197454.
[14] Cherepanov GP. Inverse problems of the plane theory of elasticity. J Appl Math Mech 1974;38:915–31. https://doi.org/10.1016/0021-8928(75)90085-4.
[15] Coelho PG, Barroca BC, Conde FM, Guedes JM. Minimization of maximal von Mises stress in porous composite microstructures using shape and topology optimization. Struct Multidiscip Optim 2021;64:1781–99. https://doi.org/10.1007/s00158-021-02942-y.
[16] Coelho PG, Fernandes PR, Rodrigues HC, Cardoso JB, Guedes JM. Numerical modeling of bone tissue adaptation – a hierarchical approach for bone apparent density and trabecular structure. J Biomech 2009;42(7):830–7. https://doi.org/10.1016/j.jbiomech.2009.01.020.
[17] Conde FM, Coelho PG, Guedes JM. Multi-material and strength-oriented microstructural topology optimization applied to discrete phase and functionally graded materials. Struct Multidiscip Optim 2022;65(4):17. https://doi.org/10.1007/s00158-022-03209-w.
[18] Conlan-Smith C, Bhattacharyya A, James KA. Optimal design of compliant mechanisms using functionally graded materials. Struct Multidisc Optim 2018;57:197–212. https://doi.org/10.1007/s00158-017-1744-y.
[19] Conlan-Smith C, James KA. A stress-based topology optimization method for heterogeneous structures. Struct Multidisc Optim 2019;60:167–83. https://doi.org/10.1007/s00158-019-02207-9.
[20] Cristello N, Kim IY. Multidisciplinary design optimization of a zero-emission vehicle chassis considering crashworthiness and hydroformability. Proc Inst Mech Eng Part D: J Autom Eng 2007;221(5):511–26. https://doi.org/10.1243/09544070JAUTO440.
[21] da Silva GA, Aage N, Beck AT, Sigmund O. Local versus global stress constraint strategies in topology optimization: a comparative study. Int J Numer Methods Eng 2021;122(21):6003–36. https://doi.org/10.1002/nme.6781.
[22] Dagum L, Menon R. OpenMP: an industry standard API for shared-memory programming. IEEE Comput Sci Eng 1998;5(1):46–55. https://doi.org/10.1109/99.660313.
[23] Deaton JD, Grandhi RV. A survey of structural and multidisciplinary continuum topology optimization: post 2000. Struct Multidiscip Optim 2014;49:1–38. https://doi.org/10.1007/s00158-013-0956-z.
[24] Deaton JD, Grandhi RV. Stress-based design of thermal structures via topology optimization. Struct Multidiscip Optim 2016;53(2):253–70. https://doi.org/10.1007/s00158-015-1331-z.
[25] Dunning PD, Brampton CJ, Kim HA. Simultaneous optimisation of structural topology and material grading using level set method. Mater Sci Technol 2015;31(8):884–94. https://doi.org/10.1179/1743284715Y.0000000022.
[26] Duysinx P, Bendsøe MP. Topology optimization of continuum structures with local stress constraints. Int J Numer Methods Eng 1998;43(8):1453–78. https://doi.org/10.1002/(SICI)1097-0207(19981230)43:8<1453::AID-NME480>3.0.CO;2-2.
[27] Duysinx P, Sigmund O (1998b) New developments in handling stress constraints in optimal material distribution. In: 7th AIAA/USAF/NASA/ISSMO Symp on Multidisciplinary Analysis and Optimization 1:1501–1509. DOI: 10.2514/6.1998-4906.
[28] Gao T, Zhang W. Topology optimization involving thermo-elastic stress loads. Struct Multidiscip Optim 2010;42(5):725–38. https://doi.org/10.1007/s00158-010-0527-5.
[29] Giraldo-Londono O, Paulino GH. PolyStress: a Matlab implementation for local stress-constrained topology optimization using the augmented Lagrangian method. Struct Multidiscip Optim 2021;63:2065–97. https://doi.org/10.1007/s00158-020-02760-8.
[30] Giraldo-Londono O, Aguilo MA, Paulino GH. Local stress constraints in topology optimization of structures subjected to arbitrary dynamic loads: a stress aggregation-free approach. Struct Multidiscip Optim 2021;64:3287–309. https://doi.org/10.1007/s00158-021-02954-8.
[31] Goyat V, Verma S, Garg RK. On the reduction of stress concentration factor in an infinite panel using different radial functionally graded materials. Int J Mater Prod Technol 2018;57(1–3):109–28. https://doi.org/10.1504/IJMPT.2018.092937.
[32] Goyat V, Verma S, Garg RK. Stress concentration reduction using different functionally graded materials layer around their hole in an infinite panel. Strength Fract Complex 2019;1:1–15. https://doi.org/10.3233/SFC-190232.
[33] Guo X, Zhang W, Zhong W. Stress-related topology optimization of continuum structures involving multi-phase materials. Comput Methods Appl Mech Engrg 2014;268:632–55. https://doi.org/10.1016/j.cma.2013.10.003.

[34] Han Y, Xu B, Duan Z, Huang X. Stress-based multi-material structural topology optimization considering graded interfaces. Comput Methods Appl Mech Eng 2022; 391(114):602. https://doi.org/10.1016/j.cma.2022.114602.

[35] Han Z, Wei K, Gu Z, Ma X, Yang X. Stress-constrained multi-material topology optimization via an improved alternating active-phase algorithm. Eng Optim 2022; 54(6):1–24. https://doi.org/10.1080/0305215X.2020.1867119.

[36] Hashin Z, Shtrikman S. A variational approach to the theory of the elastic behaviour of multiphase materials. J Mech Phys Solids 1963;11(2):127–40. https://doi.org/10.1016/0022-5096(63)90060-7.

[37] Haug EJ, Choi KK, Komkov V. Design sensitivity analysis of structural systems. Orlando: Academic Press Inc.; 1986.

[38] Holmberg E, Torstenfelt B, Klarbring A. Stress constrained topology optimization. Struct Multidiscip Optim 2013;48:33–47. https://doi.org/10.1007/s00158-012-0880-7.

[39] Hu J, Liu Y, Luo Y, Huang H, Liu S. Topology optimization of multi-material structures considering a piecewise interface stress constraint. Comput Methods Appl Mech Eng 2022;398:115274. https://doi.org/10.1016/j.cma.2022.115274.

[40] Hvejsel CF, Lund E, Stolpe M. Optimization strategies for discrete multi-material stiffness optimization. Struct Multidiscip Optim 2011;44(2):149–63. https://doi.org/10.1007/s00158-011-0648-5.

[41] Ituarte IF, Boddeti N, Hassani V, Dunn ML, Rosen DW. Design and additive manufacture of functionally graded structures based on digital materials. Addit Manuf 2019;30:100839. https://doi.org/10.1016/j.addma.2019.100839.

[42] Jung Y, Lim S, Kim J, Min S. Lightweight design of electric bus roof structure using multi-material topology optimisation. Struct Multidiscip Optim 2020;61(3): 1273–85. https://doi.org/10.1007/s00158-019-02410-8.

[43] Kang Z, Wu C, Lou Y, Li M. Robust topology optimization of multi-material structures considering uncertain graded interface. Compos Struct 2019;208: 395–406. https://doi.org/10.1016/j.compstruct.2018.10.034.

[44] Kennedy GJ. A full-space barrier method for stress-constrained discrete material design optimization. Struct Multidiscip Optim 2016;54(3):619–39. https://doi.org/10.1007/s00158-016-1428-z.

[45] Kennedy GJ, Chin TW. A sequential convex optimization method for multimaterial compliance design problems. Comput Struct 2019;212:110–24. https://doi.org/10.1016/j.compstruc.2018.10.007.

[46] Kikuchi N. Finite element methods in mechanics. CUP Archive; 1986.

[47] Kim J-H, Paulino GH. Isoparametric graded finite elements for non-homogeneous isotropic and orthotropic materials. J Appl Mech 2002;69(4):502–14. https://doi.org/10.1115/1.1467094.

[48] Koizumi M. FGM activities in Japan. Compos B: Eng 1997;28:1–4. https://doi.org/10.1016/S1359-8368(96)00016-9.

[49] Kundu RD, Li W, Zhang XS. Multimaterial stress-constrained topology optimization with multiple distinct yield criteria. Extreme Mech Lett 2022;54:101716. https://doi.org/10.1016/j.eml.2022.101716.

[50] Le C, Norato J, Bruns T, Ha C, Tortorelli D. Stress-based topology optimization for continua. Struct Multidiscip Optim 2010;41:605–20. https://doi.org/10.1007/s00158-009-0440-y.

[51] Li C, Kim IY (2015) Topology, size and shape optimization of an automotive cross car beam. Proceedings of the Institution of Mechanical Engineers, Part D: J Autom Eng 229(10):1361–1378. DOI: 10.1177/0954407014561279.

[52] Li C, Kim IY. Multi-material topology optimization for automotive design problems. Proc Institut Mech Eng Part d: J Autom Eng 2018;232:1950–69. https://doi.org/10.1177/0954407017737901.

[53] Li D, Kim IY. Multi-material topology optimization for practical lightweight design. Struct Multidiscip Optim 2018;58(3):1081–94. https://doi.org/10.1007/s00158-018-1953-z.

[54] Lipton R. Design of functionally graded composite structures in the presence of stress constraints. Int J Solids and Struct 2002;39:2575–86. https://doi.org/10.1016/S0020-7683(02)00129-4.

[55] Long K, Wang X, Gu X. Local optimum in multi-material topology optimization and solution by reciprocal variables. Struct Multidiscip Optim 2018;57(3):1283–95. https://doi.org/10.1007/s00158-017-1811-4.

[56] Lu S, Ma H, Xin L, Zuo W. Lightweight design of bus frames from multi-material topology optimization to cross-sectional size optimization. Eng Optim 2019;51(6): 961–77. https://doi.org/10.1080/0305215X.2018.1506770.

[57] Lund E. Discrete material and thickness optimization of laminated composite structures including failure criteria. Struct Multidisc Optim 2018;57:2357–75. https://doi.org/10.1007/s00158-017-1866-2.

[58] Ma G, Yang W, Wang L. Strength-constrained simultaneous optimization of topology and fiber orientation of fiber-reinforced composite structures for additive manufacturing. Adv Struct Eng 2022;25(7):1636–51. https://doi.org/10.1177/13694332221088946.

[59] Meng L, Zhang W, Quan D, Shi G, Tang L, Hou Y, et al. From topology optimization design to additive manufacturing: today's success and tomorrow's roadmap. Arch Computat Methods Eng 2019;27(8):805–30. https://doi.org/10.1007/s11831-019-09331-1.

[60] Michell AGM. The limits of economy of material in frame-structures. Philos Mag 1904;8(6):589–97. https://doi.org/10.1080/14786440409463229.

[61] Miyamoto Y, Kaisser W, Rabin BH, Kawasaki A, Ford Renée G. Functionally graded materials: design, processing, and applications. New York: Springer; 1999.

[62] Nazir A, Gokcekaya O, Billah KMM, Ertugrul O, Jiang J, Sun J, et al. Multi-material additive manufacturing: A systematic review of design, properties, applications, challenges, and 3D printing of materials and cellular metamaterials. Mater Des 2023;226:111661. https://doi.org/10.1016/j.matdes.2023.111661.

[63] Nikbakht S, Kamarian S, Shakeri M. A review on optimization of composite structures part II: functionally graded materials. Compos Struct 2019;214:83–102. https://doi.org/10.1016/j.compstruct.2019.01.105.

[64] Opgenoord MMJ, Willcox KE. Design for additive manufacturing: cellular structures in early-stage aerospace design. Struct Multidiscip Optim 2019;60(2): 411–28. https://doi.org/10.1007/s00158-019-02305-8.

[65] París J, Navarrina F, Colominas I, Casteleiro M. Block aggregation of stress constraints in topology optimization of structures. Adv Eng Softw 2010;41(3): 433–41. https://doi.org/10.1016/j.advengsoft.2009.03.006.

[66] París J, Navarrina F, Colominas I, Casteleiro M. Improvements in the treatment of stress constraints in structural topology optimization problems. J Comput Appl Math 2010;234:2231–8. https://doi.org/10.1016/j.cam.2009.08.080.

[67] Radman A, Huang X, Xie YM. Topology optimization of functionally graded cellular materials. J Mater Sci 2013;48:1503–10. https://doi.org/10.1007/s10853-012-6905-1.

[68] Ramani A. Multi-material topology optimization with strength constraints. Struct Multidiscip Optim 2011;43(5):597–615. https://doi.org/10.1007/s00158-010-0581-z.

[69] Rozvany GIN. Aims, Scope, history and unified terminology of computer-aided topology optimization. Struct Multidisc Optim 2001;21:90–108. https://doi.org/10.1007/s001580050174.

[70] Rozvany GIN. A critical review of established methods of structural topology optimization. Struct Multidiscip Optim 2009;37(3):217–37. https://doi.org/10.1007/s00158-007-0217-0.

[71] Saleh B, Jiang J, Fathi R, Al-hababi T, Xu Q, Wang L, et al. 30 Years of functionally graded materials: An overview of manufacturing methods, Applications and Future Challenges. Compos B: Eng 2020;201:108376. https://doi.org/10.1016/j.compositesb.2020.108376.

[72] Sanders ED, Aguilo MA, Paulino GH. Multi-material continuum topology optimization with arbitrary volume and mass constraints. Comput Methods Appl Mech Eng 2018;340:798–823. https://doi.org/10.1016/j.cma.2018.01.032.

[73] Sburlati R. International Journal of Solids and Structures Stress concentration factor due to a functionally graded ring around a hole in an isotropic plate. Int J Solids Struct 2013;50:3649–58. https://doi.org/10.1016/j.ijsolstr.2013.07.007.

[74] Sburlati R, Atashipour SR, Atashipour SA. Reduction of the stress concentration in a homogeneous panel with hole by using a functionally graded layer. Compos Part B 2014;61:99–109. https://doi.org/10.1016/j.compositesb.2014.01.036.

[75] Senhora FV, Giraldo-Londono O, Menezes IFM, et al. Topology optimization with local stress constraints: a stress aggregation-free approach. Struct Multidiscip Optim 2020;62:1639–68. https://doi.org/10.1007/s00158-020-02573-9.

[76] Sigmund O. Morphology-based black and white filters for topology optimization. Struct Multidiscip Optim 2007;33:401–24. https://doi.org/10.1007/s00158-006-0087-x.

[77] Sigmund O, Maute K (2013) Topology optimization approaches. Struct Multidiscip Optim 48:1031–1055. DOI: 10.1007/s00158-013-0978-6.

[78] Stolpe M, Svanberg K. An alternative interpolation scheme for minimum compliance topology optimization. Struct Multidiscip Optim 2001;22(1):116–24. https://doi.org/10.1007/s001580100129.

[79] Stump F, Silva E, Paulino G. Optimization of material distribution in functionally graded structures with stress constraints. Commun numer methods eng 2007;23: 535–51. https://doi.org/10.1002/cnm.910.

[80] Suresh S, Mortensen A (1988) Fundamentals of Functionally Graded Materials: Processing and Thermomechanical Behavior of Graded Metals and Metal-Ceramic Composites. IOM Communications Ltd. London. DOI: 10.1179/imr.1997.42.3.85.

[81] Svanberg K. The method of moving asymptotes: a new method for structural optimization. Int J Numer Methods Eng 1987;24:359–73. https://doi.org/10.1002/nme.1620240207.

[82] Swan CC, Kosaka I. Voigt-Reuss topology optimization for structures with linear elastic material behaviors. Int J Numer Methods Eng 1997;40:3033–57. https://doi.org/10.1002/(SICI)1097-0207(19971030)40:20<3785::AID-NME240>3.0.CO;2-V.

[83] Taheri AH, Suresh K. An isogeometric approach to topology of multi-material and functionally graded structures. Int J Num Meth Eng 2017;109:668–96. https://doi.org/10.1002/nme.5303.

[84] Tamijani AY. Stress and stiffness-based topology optimization of two-material thermal structures. Comput Struct 2021;256:106641. https://doi.org/10.1016/j.compstruc.2021.106641.

[85] Taylor J, Bendsøe M. An interpretation of min-max structural design problems including a method for relaxing constraints. Int J Solids Struct 1984;20:301–14. https://doi.org/10.1016/0020-7683(84)90041-6.

[86] Vermaak N, Michailidis G, Parry G, Estevez R, Allaire G, Bréchet Y. Material interface effects on the topology optimization of multi-phase structures using a level set method. Struct and Multidisc Optim 2014;50(4):623–44. https://doi.org/10.1007/s00158-014-1074-2.

[87] Wang MY, Wang X, Guo D. A level set method for structural topology optimization. Comput Methods Appl Mech Eng 2003;192(1–2):227–46. https://doi.org/10.1016/S0045-7825(02)00559-5.

[88] Woischwill C, Kim IY. Multimaterial multijoint topology optimization. Int J Numer Methods Eng 2018;115(13):1552–79. https://doi.org/10.1002/nme.5908.

[89] Xia Q, Wang MY. Simultaneous optimization of the material properties and the topology of functionally graded structures. Comput Aided Des 2008;40:660–7. https://doi.org/10.1016/j.cad.2008.01.014.

[90] Xu S, Liu J, Zou B, Li Q, Ma Y. Stress constrained multi-material topology optimization with the ordered SIMP method. Comput Methods Appl Mech Engrg 2021;373:113453. https://doi.org/10.1016/j.cma.2020.113453.

[91] Yang Q, Gao C-F, Chen W. Stress analysis of a functional graded material plate with a circular hole. Arch Appl Mech 2010;80:895–907. https://doi.org/10.1007/s00419-009-0349-3.
[92] Yang Q, Gao C-F. Reduction of the stress concentration around an elliptic hole by using a functionally graded layer. Acta Mechanica 2016;227:2427–37. https://doi.org/10.1007/s00707-016-1620-7.
[93] Young WC, Budynas RG, Roark RJ. Roark's Formulas for Stress and Strain. New York: McGraw-Hill; 2002.
[94] Zuo W, Saitou K. Multi-material topology optimization using ordered SIMP interpolation. Struct Multidiscip Optim 2017;55:477–91. https://doi.org/10.1007/s00158-016-1513-3.